Studies of cosmic ray events in ATLAS sTGC muon chamber prototypes

Félix Léger
Department of Physics
McGill University

11th September 2017

A thesis submitted to McGill University in partial fulfilment of the requirements of the degree of M.Sc.

Abstract

Four years after its first long shutdown in 2015, the Large Hadron Collider (LHC) will be shut down once more for a luminosity upgrade. During that time, the ATLAS detector on the LHC ring will also follow an upgrade program, one upgrade being the replacement of the Small Muon Wheels for a New Small Wheel containing small-strip Thin Gap Chambers (sTGCs). The sTGCs built in Canada will be tested at McGill University before their installation in ATLAS. A testing facility has been constructed and a $40 \times 60\text{cm}^2$ sTGC prototype has been used to deliver preliminary measurements from cosmic rays. This thesis will present the development of a robust tracking algorithm which can handle extra clusters and multiple tracks in an sTGC detector. This algorithm also categorizes events based on their number of clusters and tracks. By modifying the trigger time window of the sTGC prototype, the evolution of the distribution of events over this categorization is shown.

Résumé

Quatre ans après son premier arrêt en 2015, le Grand Collisionneur Hadronique (LHC) sera mis en arrêt une fois de plus pour augmenter sa lumonisité. Pendant ce temps, le détecteur ATLAS situé sur le cercle du LHC suivra lui aussi un programme visant son amélioration. Un des changements sera le remplacement des petites roues à muons pour de nouvelles petites roues contenant des Chambres Minces à petites bandes (sTGCs). Les sTGC seront construites au Canada et seront testées à l'université McGill avant d'être installées dans ATLAS. Un laboratoire de test a été construit à cette fin et un prototype sTGC de $40 \times 60\text{cm}^2$ a été utilisé pour faire des mesures préliminaires de rayons cosmiques. Cette thèse présentera le développement d'un algorithme robuste permettant de reconstruire des événements contenant plusieurs points et traces dans un détecteur sTGC. Cet algorithme peut aussi catégoriser ces événements en se basant sur leur nombre de points et de traces. En modifiant le temps de déclenchement d'acquisition de données du prototype sTGC, l'évolution de la distribution d'événements dans les différentes catégories est présentée.

Acknowledgements

This section may seem like it should be the easiest one to write, and yet, I pictured it so many times in my mind through my journey as a physicist that I don't know where to begin. I wish to give my deepest thanks to these people for believing in me and creating some of my most vivid memories.

First of all, thanks to my supervisors Steven Robertson and Andreas Warburton for all your guidance and your time. You created an environment where I could go as far as my imagination would, even through different time zones, and for this I am truly grateful.

Thanks to the sTGC lab team, in particular Andrée Robichaud-Véronneau, Benoît Lefebvre, Lévis Pépin and Robert Keyes. Your help was invaluable, and wherever your journey takes you, your future team will be lucky to have you.

Thanks to Jonathan Larochelle and Martin Klassen for their help with the GEANT4 analysis.

Thanks to all the great friends I made along the way: Alessandro, Andrea, Annabelle, Bryce, Helena, Isabelle, Kays, Matthew, Megan, Sébastien, Shalu, Shreya, Tariq, Waleed, Wei, I owe you all a beer! A special thank you to all my friends at University of Montreal, who helped me build the man I am today. Je ne vous oublierai jamais.

Thanks to my family for always believing in me and giving me the chance to shoot for the stars. Hi mom, I made it! I hope you have strong magnets on your fridge, this is a heavy one.

Finally, a special thank you to Gabrielle, for everything you do, and everything you've done. I couldn't wish for a better partner.

Contents

List of Figures

List of Tables

1 Introduction

What are the building blocks of the matter that constitutes our universe? To this day, physicists are still being challenged by this timeless question. A very successful theory, known as the Standard Model of particle physics, has been developed in the mid-1970s [1]. The theory, however, is imperfect. Essentially, it lacks robustness at very high energies. It also brought its fair share of new questions with its inception that are still unanswered. For example, why is there more matter than anti-matter in the universe? What is Dark Matter? How is the mass of a fundamental particle determined?

One of the experiments that aims to answer these questions is the ATLAS experiment [2]. At 25m high and 44m wide, this cylindrical particle detector is the largest detector situated on the ring of the Large Hadron Collider (LHC) [3], itself located at CERN on the Swiss-France border. The LHC collides protons moving at 0.99999999 times the speed of light in the center of the ATLAS detector. This tremendous energy (up to $\sqrt{s} = 13$TeV in the center of the collision) is necessary to probe the minuscule scale of fundamental particles. During the second long shutdown (LS2) of the LHC planned in 2019, the ATLAS detector will follow an upgrade program to cope with a higher luminosity. An important part of this upgrade will be to replace the current Muon Small Wheels, made of Thin Gap Chambers (TGC), with the Muon New Small Wheels [4], made of Micromesh Gaseous Structure detectors and small-strip Thin Gap Chambers (sTGC).

The sTGC detectors will be constructed by five different countries, including Canada. A team of physicists at McGill University will be responsible for testing the Canadian sTGC detectors, in particular their spatial resolution and their hit efficiency. A testing environment has been developed at McGill in preparation for the arrival of the sTGC modules [5]. A $40 \times 60\text{cm}^2$ sTGC prototype using cosmic rays for detection has been used in preparation for the real sTGC modules. This prototype is able to record tracks from particles that traverse it. While most measured cosmic ray events contain a single track, some events can contain two or more. The rate of events with two tracks has been measured and it was concluded that these events are most probably due to delta-rays (which will be defined in chapter 2) or similar effects. Since the purpose of the lab is to make a precise characterization of the chamber efficiencies based on clean single muon events, it is important to understand the detector environment, and in particular the rate of background and/or fake hits. This thesis presents developments towards categorizing double track events measured in a prototype sTGC quadruplet in the Canadian sTGC testing facility at McGill, as well as all issues that can impact the performance of the track reconstruction for the purposes of efficiency measurement.

The thesis is outlined as follows. Chapter 2 describes the Standard Model and the relevant elements needed for this analysis. Chapter 3 describes the LHC, the ATLAS detector, as well as the Canadian sTGC test bench. Chapter 4 describes the analysis techniques used. Chapter 5 shows the results of this analysis and discusses these results. Finally, chapter 6 concludes the thesis and provides outlook for future work.

2

Theoretical Background

2.1 The Standard Model of Particle Physics

The Standard Model (SM) of particle physics describes the interactions of forces and matter in our universe. It is the result of Glashow's unification of the electromagnetic and weak interactions [6] in which Weinberg [7] and Salam [8] incorporated the Higgs mechanism [9]. The model describes three of the four fundamental forces in the universe (weak, strong and electromagnetic interactions). All observed fundamental particles and their interactions (including bound states) are broadly consistent with this model. The modern form of the SM was adopted in 1974 along with the current theory of the strong interaction. This followed from the proposition of asymptotic freedom [10] and the experimental confirmation that hadrons were composed of quarks with fractionary charges [11]. Illustrated in figure 2.1, the particles of the SM are divided into two types: fermions and bosons. Bosons are particle that follow Bose-Einstein statistics and have integer spin, whereas fermions obey Fermi statistics and have $n + \frac{1}{2}$ spin, where n is an integer.

Fermions are populated by two groups of particles, quarks and leptons, of which there are three generations (represented by the first three columns). In these

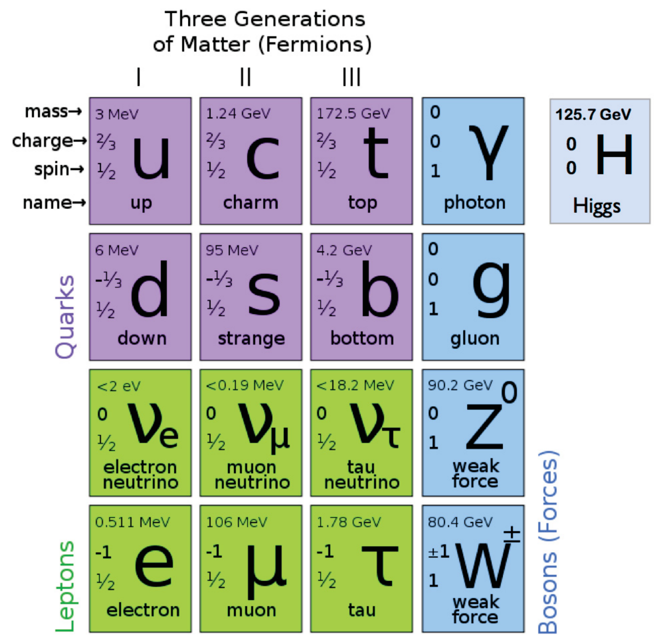

Figure 2.1: The particle content of Standard Model [12]

columns, mass increases from left to right. Everyday matter is made of the first column. Indeed, an atom contains protons and neutrons, which are formed themselves by quarks (respectively uud and udd), and electrons. Leptons in the second column include muons, which are ∼206 times more massive than an electron [13]. They have a mean lifetime of $\sim 2.2\mu$s, after which they decay most frequently to an electron, an electron antineutrino and a muon neutrino [14]. However, because of time dilation, muons can survive for longer times in our reference frame if they are ultrarelativistic.

As for vector bosons (not the Higgs, which is a scalar boson), these can be interpreted as carriers of the fundamental forces. The photon carries the electromagnetic force, the gluon carries the strong force and the $W^{\pm}$ and Z bosons (respectively discovered in 1983 by the UA1 [15] and the UA2 [16] collaborations) carry the weak force. The Higgs boson, which is the only scalar particle (spin 0), is a quantum excitation of the Higgs field, which interacts with SM particles to give them mass. Gravity is not included in the SM as it contributes very little at the atomic scale [17].

Experiments have tested the SM very precisely over many energy scales (from eV to TeV). The successes of the SM include, but are not limited to, predicting the existence of the top quark, the gluon and the W and Z bosons before these particles were detected experimentally. It also successfully predicted the existence of the Higgs boson nearly 50 years before its discovery [18]. However, the SM is not a complete description of nature in its current state. For instance, it does not explain why the weak force is 10^{24} times stronger than gravity (also known as the hierarchy problem). Furthermore, the model requires 26 [19] seemingly arbitrary valued constants which cannot be satisfyingly be explained. These constants are:

- $m_u, m_d, m_c, m_s, m_t, m_b$, the masses of the six quarks
- $m_e, m_{\nu_e}, m_\mu, m_{\nu_\mu}, m_\tau, m_{\nu_\tau}$, the masses of the six leptons
- m_H, the mass of the Higgs boson
- vev_H, the vacuum expectation value of the Higgs field
- The three mixing angles and the CP-violating phase of the Cabibbo-Kobayashi-Maskawa (CKM) matrix
- The three mixing angles and the CP-violating phase of the Pontecorvo-Maki-Nakagawa-Sakata (PMNS) matrix
- $g_{U(1)}$, the U(1) coupling constant
- $g_{SU(2)}$, the SU(2) coupling constant

- g_3, the coupling constant of the strong interaction
- Λ, the cosmological constant

A clear structure can be observed for the mass values and the mixing angles, but their origin is not explained by the SM. The model also explains only about 5% of the energy present in the universe. Roughly 26% of this total energy should be Dark Matter, which would interact weakly with matter from the SM. While massive neutrinos are great dark matter candidates, they do not fit with cosmology experiments [20]. Hence, if dark matter is to be explained by particle physics, then the relevant particle(s) are from beyond the SM.

Many theories expand Beyond the Standard Model (BSM) and aim to provide a solution for these problems. For example, since these problems relate to the electroweak scale ($\sim$ TeV), it seems "natural" the solution would also appear at this scale. By colliding particles at the LHC at high enough energies, new particles could be found. For example, Supersymmetry (SUSY) suggests that every particle in the SM could have a supersymmetric partner [21]. If SUSY particles were to be observed, this would fix the hierarchy problem, gauge coupling unification, and provide dark matter candidate particles, among other things. Many SUSY theories exist, all with different parameters and specifications.

2.2 Cosmic Rays

2.2.1 Discovery

Cosmic rays were discovered by Victor Hess in 1912. At that time, the electrometer had just been invented by Theodor Wulf in 1909 [22]. The device would sponta-

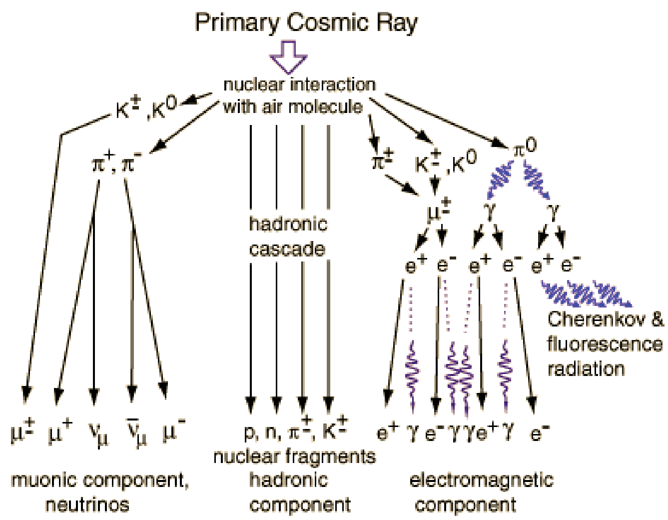

Figure 2.2: The secondary particles of a cosmic ray decay, resulting from the interaction with nuclei from atmospheric atoms [23]. Pions and kaons usually decay muonically [14].

neously discharge in the presence of radioactive materials, with the rate of discharge being linearly related to the level of radiation inside the apparatus. The issue was that discharges were observed even in the absence of radioactive materials and even when the electrometer was shielded by heavy metals, like lead. It was theorized that this background radioactivity came from the Earth itself. To test this theory, Hess flew to an altitude of 5.3 km in a free balloon flight, bringing with him an electrometer. Surprisingly, he found that radiation levels increased with altitude. At his maximum height, he measured levels of radiation four times higher than at ground level. He ruled out the Sun as the source of this radiation by making his flight during a near-total eclipse. His conclusion was that radiation (later named "cosmic rays") came from space, had great penetrating power and entered the Earth's atmosphere from above.

Modern experiments determined that cosmic rays are made of highly energetic particles (roughly 90% protons and 9% alpha particles [24]) that come from outside the Solar System, and sometimes even the Milky Way. Cosmic rays of 1 GeV reach the top of the Earth's atmosphere at a rate of 1.8×10^4kHz/m^2 [14]. Observations from the Fermi space telescope suggest they primarily originate from supernovae of massive stars [25]. Upon interacting with the Earth's atmosphere, these particles produce secondary particles, mostly muons (μ), muon neutrinos (ν_μ), electrons (e) and photons (γ), as illustrated in figure 2.2. Because electrons emit photons via Bremsstrahlung, secondary electrons from cosmic rays do not travel far into the atmosphere. As for muons, due to their greater mass compared to electrons, they emit considerably less via Bremsstrahlung, and interact with the atmosphere mostly via ionization. Thus, secondary cosmic muons can be detected in underground mines due to their ability to deeply penetrate matter. However, because of their short lifetime, relativistic time dilation is needed for them to reach the earth. At sea level, muons are the only charged particles remaining after the decay of secondary cosmic ray particles.

2.3 Muon interaction with matter (δ-rays)

Most secondary cosmic muons are produced high in the atmosphere at typically 15 km [14][1]. Due mostly to ionization, they will lose about 2 GeV before reaching the ground. Their mean energy when they reach sea level is $\approx$ 4GeV and their intensity is $I \approx 1\text{cm}^{-2}\text{min}^{-1}$. Their overall angular distribution is $\propto \cos^2\theta$, where θ is the zenith angle.

As these muons traverse matter, their energy loss can be written as a function of matter they traverse:

[1]This section is adapted from the PDG

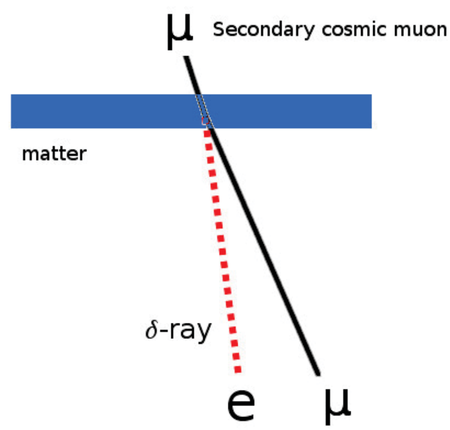

Figure 2.3: A muon interacting with matter has a probability of knocking off an electron from an atom, which results in a δ-ray. The muon is only slightly deviated. The electron trajectory is correlated with the muon.

$$\frac{dE_\mu}{dX} = -a - bE_\mu \tag{2.1}$$

where a is the ionization loss and b is the fractional energy loss due to the three processes stated above. These parameters slowly vary with energy. In rock with $A = 22$, $Z = 11$, $\rho = 2.65\frac{g}{\text{cm}^3}$, $\frac{a}{b} \approx 500\text{GeV}$. Equation 2.1 can be integrated to express the average muon energy E_μ after traversing a thickness X of matter:

$$E_\mu = \left(E_{\mu_0} - \frac{a}{b}\right) e^{-bX} + \frac{a}{b} \tag{2.2}$$

When a secondary cosmic muon penetrates matter, its energy is such that it can knock off an electron from an atom of that matter and continue its course (figure 2.3). The electron resulting from this interaction is called a δ-ray [26]. While this radiation cannot travel as far as a muon due to Bremsstrahlung radiation, it can start its course with significant energy to be detected by a particle detector. Since the muon responsible for the creation of a δ-ray is about 200 times more massive than the electron and ultrarelativistic, the muon's trajectory is only slightly deviated by the collision. As a result, due to momentum conservation, the δ-ray should follow a trajectory closely related to the muon's.

To summarize, muons are particles of the Standard Model that can be detected when they interact with matter. Cosmic rays provide a constant source of muonic radiation on Earth. Examples of particle physics experiments which use muon detection will be given in the next chapter.

3

Experimental Setup

3.1 The Large Hadron Collider

Initially started in September 2008, the LHC is the world's current largest and most powerful particle accelerator. The particles that are collided in the LHC are protons (and sometimes heavy ions). They are accelerated by a succession of machines until they reach a velocity 3.1 m/s below the speed of light (c). The acceleration process starts with a bottle of hydrogen gas, where an electric field is used to strip the electron from hydrogen atoms, which yields the proton that will later be used for collisions [27]. These protons are then fed into the Linac 2, the first accelerator in the chain, which accelerates them to the energy of 50MeV. They are then fed into a bigger accelerator, the Proton Synchrotron Booster (PBS), which accelerates them to an energy of 1.4GeV. The process continues, with protons being accelerated to 25GeV by the Proton Synchrotron (PS), followed by the Super Proton Synchrotron (SPS) where they reach 450GeV. It is then that the protons reach their final destination, the LHC ring, where they are divided into two separate pipes, one where they travel clockwise, and the other where they travel anticlockwise. The highest recorded energy of a proton beam at LHC is 6.5TeV. The LHC ring containing the proton beams is 27km in circumference and is located 100m under the Swiss-French border. It produces proton collisions at an energy up to 14TeV (each colliding beam has an energy of up to 7TeV), with a design luminosity of 10^{34}cm^{-2}s^{-1}. A beam has up to 2808 bunches, with 1.15×10^{11} protons per bunch, a peak luminosity of 10^{34}cm^{-2}s^{-1} and a bunch spacing of 24.95 ns [28] (design specs). A primary goal of the LHC was to find and study the properties of the Higgs boson. Its present goals are to characterize the SM, in particular the Higgs sector, at the electroweak scale, and to continue to search for evidence of new physics at the TeV scale.

The LHC has four crossing points (figure 3.1) around which are positioned independent particle detectors, each designed for a certain type of research:

- ATLAS: A general-purpose detector designed to study a wide range of physics. Now that it discovered the Higgs boson, it is used to make precision measurements of the SM, particularly for events containing jets and charged leptons.

- ALICE: A heavy-ion detector designed to study the physics of strongly interacting matter at extreme energy densities.

- CMS: A general-purpose detector that has the same scientific goals as the ATLAS detector, but uses different technical solutions and a different magnet-system design.

- LHCb: A detector designed to study the b quark to investigate slight differences between matter and antimatter.

The LHC started its operations on September 10 2008, but suffered a magnet quench incident 9 days later, which delayed initial testing by 14 months [29]. The

Figure 3.1: Aerial view of the LHC. The two proton beams travel in opposite directions. The four main experiments (ATLAS, CMS, Alice and LHCb) lie along the accelerator's circumference and are located in the interaction regions (IR) where the beams cross.

first operational run (known as Run-1) lasted from 2009 to 2013. It initially set the record for the highest-energy particle accelerator by producing proton beams of 1.18TeV on November 30 2009, beating the previous record held during 8 years by the Tevatron (0.98TeV per beam). The energy was ramped-up once more to reach 3.5TeV per beam on March 30 2010. A short break in the fourth quarter of 2011 was made to increase the beam energy to 4TeV. After the discovery of the Higgs boson in July 2012, the LHC was once more shut down, this time to make upgrades in order to collide protons beams of up to 7TeV per beam. It restarted its operations in 2015 after a two-year break, producing beams of 6.5TeV. Another long shut down, planned for 2018, will enable increasing once again the beam energy and luminosity of the LHC. As a result, the four detectors located on the LHC ring will also have to be upgraded to cope with the foreseen higher luminosity. In total, the LHC delivered 5.6fb^{-1} of data in terms of integrated luminosity between 2010 and 2011, and about 42fb^{-1} between 2015 and June 2017. By 2035, the LHC plans to have delivered 3000fb^{-1} of data.

3.2 ATLAS

ATLAS (A Toroidal LHC ApparatuS, figure 3.2) is a multipurpose detector located on the ring of the LHC [2]. It is cylindrically symmetric around the interaction point and has near 4π solid angle coverage. The whole detector is 25m in diameter and 46m in length and weighs 7000 tonnes. It has three main detecting regions: the inner detector, the calorimeter and the muon spectrometer. During LHC operations, proton bunches cross at a rate of 40MHz, which amounts to $\sim 10^9$ proton-proton collisions per second. Since the rate of data production is too high to be saved, a trigger system is used to select which events will be written to permanent storage for offline analysis.

The ATLAS coordinate system has its origin at the nominal proton-proton interaction point, with the z-axis resting along the beam direction. The x-y plane is perpendicular to the beam direction, with the x-axis pointing towards the center of the LHC ring and the y-axis pointing upwards. The azimuthal angle ϕ is measured around the beam axis, and the polar angle θ is the angle from the beam axis. A commonly used spatial coordinate is the pseudorapidity, defined as:

$$\eta = -\ln\left(\tan\left(\frac{\theta}{2}\right)\right) \tag{3.1}$$

The use of η is preferred over the polar angle θ, because particle production is constant as a function of η and because differences in η are Lorentz invariant.

3.2.1 The Inner Detector

The inner detector (ID) is the closest to the interaction point, positioned a few centimeters from the beam axis. It covers $|\eta| < 2.5$ and consists of three indepen-

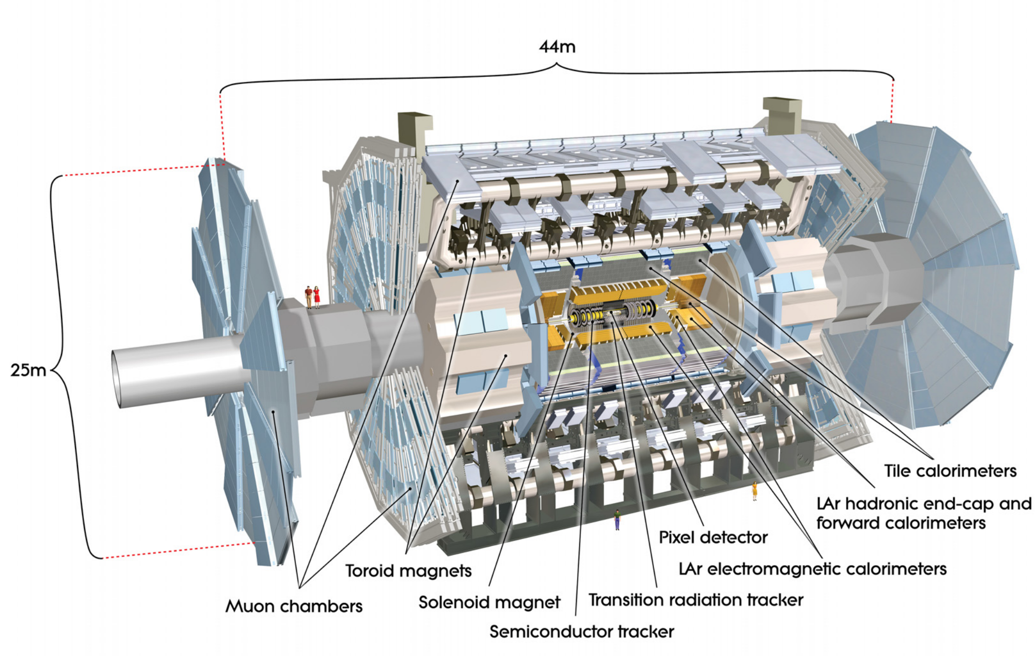

Figure 3.2: An illustration of the ATLAS detector [30]. It is 25 m in height, 44 m in length and weighs approximately 7000 tonnes.

dent but complementary sub-detectors: a silicon pixel detector, a semi-conductor tracker (SCT), and a transition radiation tracker (TRT), as shown in figure 3.3. It is immersed in a 2 T axial magnetic field provided by a thin superconducting solenoid mounted around the ID. The magnetic field provided by the solenoid is used to curve the trajectory of charged particles, which reveals both the charge and the momentum of the particles (respectively from the direction and the degree of curvature of the trajectory).

The Pixel Detector

The pixel detector is divided in 1,744 modules, each measuring $2 \times 6\text{cm}^2$, laid over three concentric layers and three disks on each end-cap. A pixel module contains 47,232 pixels (144 columns, 328 rows), and an individual pixel is $50 \times 400\mu\text{m}^2$ (ex-

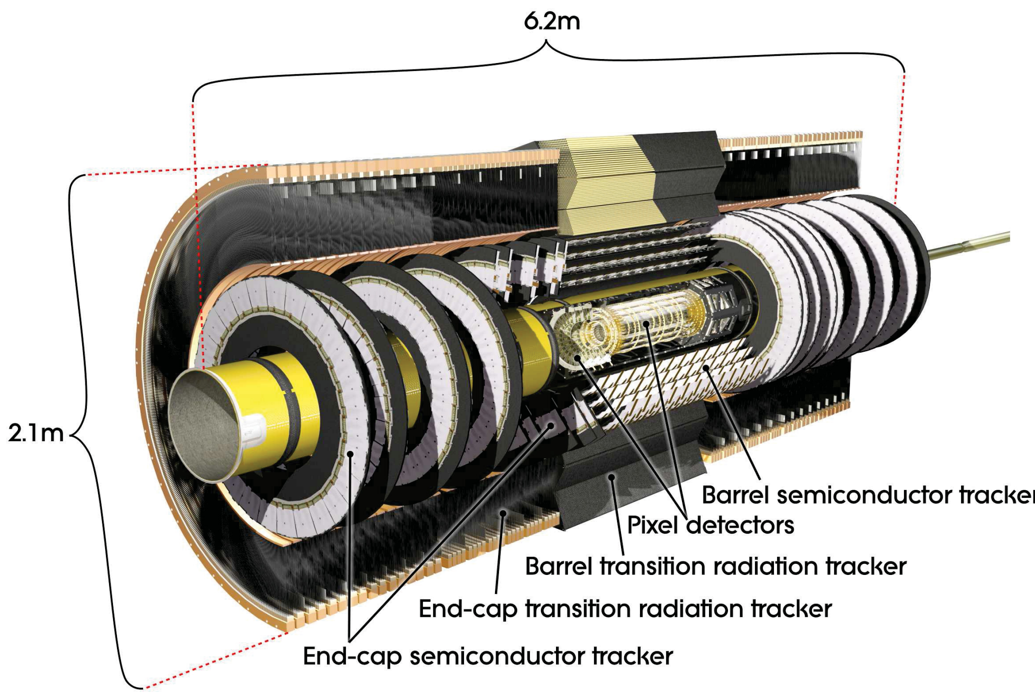

Figure 3.3: Illustration of the ATLAS inner detector.

cept at the front-end region of a module, where it is instead $50 \times 600 \mu\text{m}^2$). This high granularity is necessary to track the charged particles since most tracks resulting from the proton-proton collision are very close to each other.The spatial resolution of individual pixel modules has been estimated at 12μm in a test beam, and it was also found that 80% of the tracks have a single pixel hit in a module [31, 32].

The Semi-Conductor Tracker

Situated in the middle of the ID, the SCT has a similar concept and function to the pixel detector, but covers a larger area. Because the radiation level and the charged particle density is lower away from the interaction point, strip silicon detectors are used instead of pixels in the SCT because cost less, are easier to produce, and are overall more practical. The SCT is made of 4,088 modules and uses silicon strips that are 80μm $\times$ 12cm. As a whole, the strips have a position resolution of 17μm in $R - \phi$ and 580μm in R [33]. The SCT is the most critical part of the ID, since it is able to cover a larger area than the pixel detector with more sample points while maintaining a similar position resolution.

The Transition Radiation Tracker

The outermost component of the ID, the TRT is a detector made of 298,304 polyimide drift straw tubes of 4mm diameter. These straws are 144cm long for the barrel and 37cm long for the end-caps and contain a 31μm coaxial tungsten anode wire. To operate the TRT, these straws must be filled with a gas mixture of 70% Xe, 27% CO_2 and 3% O_2 and the cathodes must be operated at $-1,530$V to give a gain of 2.5×10^4. When a charged particles passes through the straw, it ionizes the gas and produces free electrons that will drift towards the anode wire. This drift is used as a signal to determine the position of the charged particle. On average, the TRT measures 36 hits per track, which improves the momentum resolution over $|\eta| < 2.0$ and electron identification complementary to that of the calorimeter. The TRT provides a 130μm resolution for charged particles at $|\eta| < 2$ and a transverse momentum of $p_T > 0.5$GeV$/c$ [34]. It can be used to detect electrons and positrons, because transition radiation is greatest for ultrarelativistic particles (electrons and positrons being very light, they can travel very fast).

3.2.2 The Calorimeters

The calorimeters enclose the ID and the solenoidal magnet. They cover a range of $|\eta| < 4.9$. Their primary purpose is to measure the total energy of particles by absorbing them completely. As shown in figure 3.4, there are two calorimeter sys-

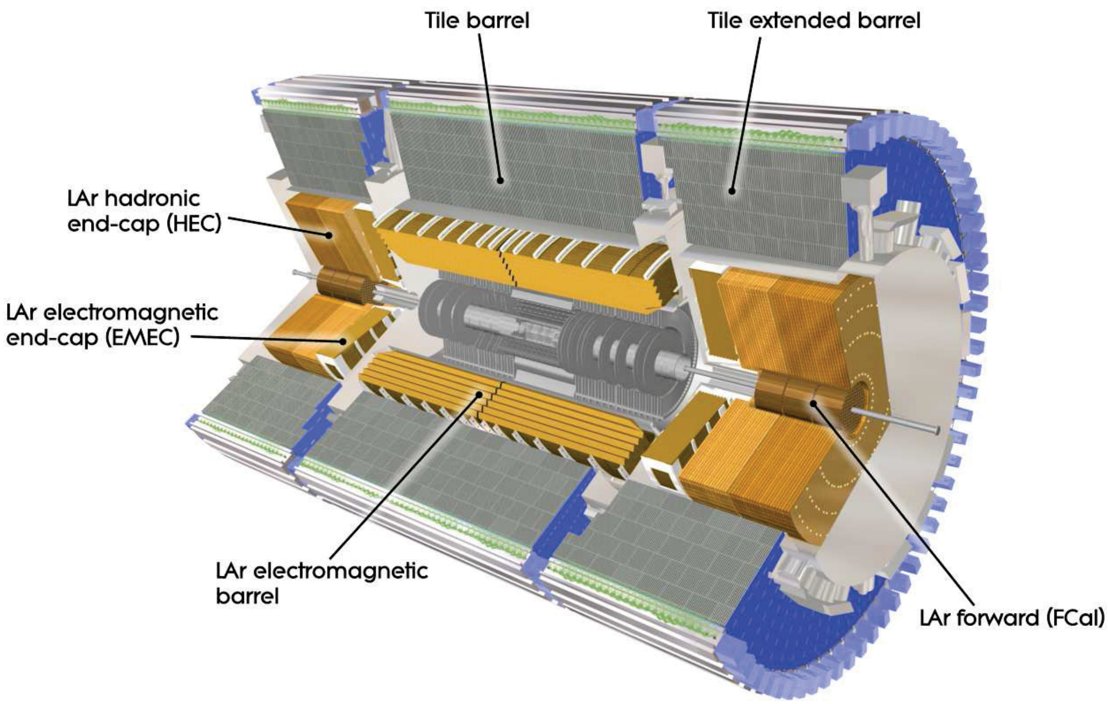

Figure 3.4: Illustration of the ATLAS calorimeter system.

tems: the electromagnetic (EM) calorimeter and the hadron calorimeter (HCAL). Being sampling calorimeters, they have layers of absorption (passive medium) interspersed with layers of detection (active medium). The absorption layers produce particle showers, of which the shape is sampled by the detection medium (and so on).

Electromagnetic Calorimeter

The EM calorimeter covers $|\eta| < 3.2$ and is able to absorb and measure the energy of particles that interact electromagnetically, such as photons and electrons. The absorption layers are made of lead, while the sampling layers are filled with liquid argon (LAr). To provide full ϕ coverage (no cracks in the EM calorimeter), these

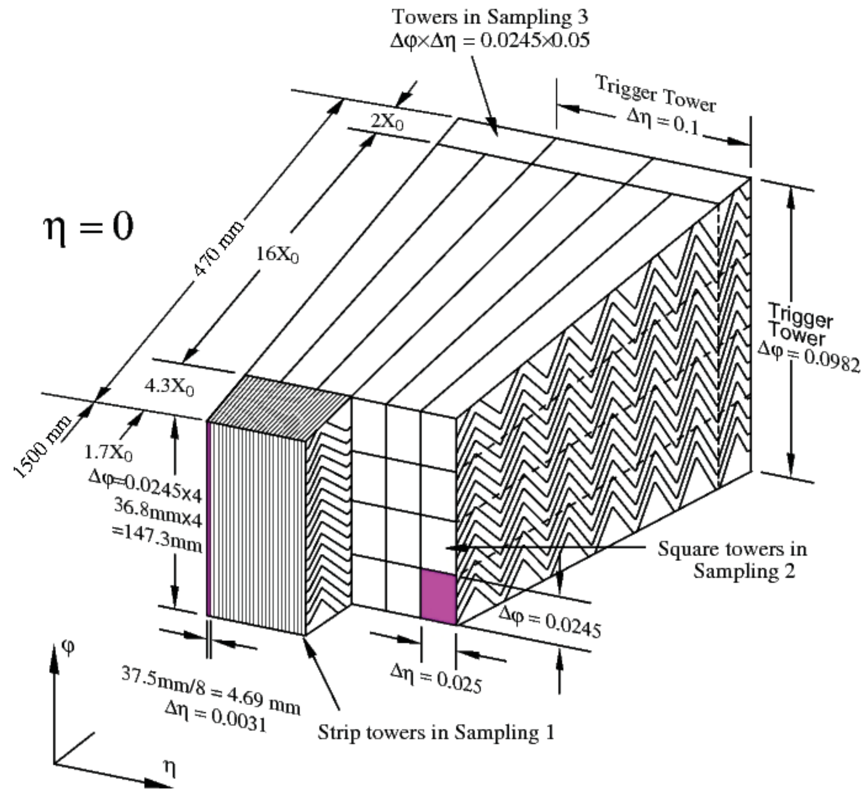

Figure 3.5: Sketch of a barrel module of the EM calorimeter where the accordion geometry is shown [2].

layers follow an accordion geometry (see figure 3.5).

Hadron Calorimeter

The HCAL wraps around the EM calorimeter and as a whole covers the region up to $|\eta| = 4.9$. It absorbs energy from strongly-interacting particles that make it through the EM calorimeter (primarily hadrons). The HCAL is divided into three sections: the tile calorimeter (barrel), the hadronic end-cap calorimeter (HEC) and the forward calorimeter (FCal). The tile calorimeter reaches up to $|\eta| < 1.7$ and uses iron plates as absorber and plastic scintillating tiles as the active material [35].

The HEC and the FCal cover a region of $1.5 < |\eta| < 3.2$ and $3.1 < |\eta| < 4.9$ respectively and are both use copper as absorber[1] and liquid-argon as active material.

3.2.3 The Muon Spectrometer

The muon spectrometer (MS), pictured in figure 3.6, surrounds the calorimeter section. It is designed to detect charged particles that make it through the barrel and end-caps of the calorimeter (mostly muons). For a pseudorapidity range of $|\eta| < 2.7$ it is used to measure the momentum of these particles, and it is also used for triggering purposes for a range of $|\eta| < 2.4$. Three concentric layers of chambers form the barrel region, at $R = 5, 7.5$ and 10m, and three layers form both end-caps (these layers being referred to as "wheels"), respectively placed at $z = \pm 7.4, \pm 14$ and ± 21.5m. Three large superconducting air-core toroid magnets, each with eight coils, provide a magnetic field of 0.5T in the barrel, while the end-caps have a magnetic field of 1T. These magnetic fields are used to bend muon tracks in order to allow them a more precise momentum measurement. The MS in its current state currently uses four different detector types:

- Muon Drift Tubes (MDT): Used for precision tracking. Covers $|\eta| < 2.7$ ($|\eta| < 2.0$ for the innermost layer)
- Cathode Strip Chambers (CSC): Used for precision tracking. Covers $2.0\,|\eta| < 2.7$
- Resistive Plate Chambers (RPC): Used for triggering, and as a second coordinate for the MDT measurement. Covers $|\eta| < 1.05$

[1] The FCal also contains 2 layers of tungsten

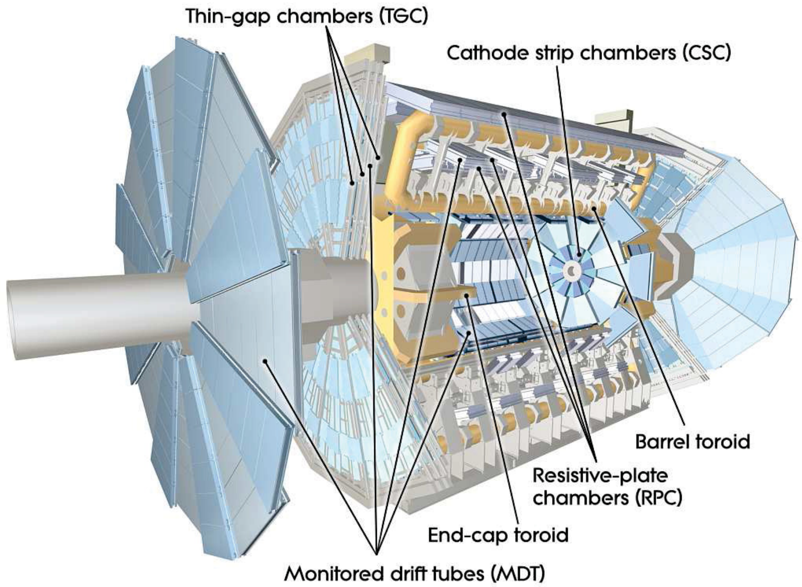

Figure 3.6: Illustration of the ATLAS muon spectrometer. The different detector types used in the MS are identified.

- Thin Gap Chambers (TGC): Used for triggering, and as a second coordinate for the MDT measurement. Covers $1.05 < |\eta| < 2.7$

The current inner end-caps, known as the muon Small Wheels (SW), will be upgraded during the next long shutdown of the LHC as part of the ATLAS upgrade program. They are currently made of CSC, MDT and TGC detectors, but will be replaced by the New Small Wheel (NSW) which uses small-Strip Thin Gap Chambers (sTGC) and MICROMEGAS (MICROMEsh GAseous Structure), as discussed in section 3.3. In particular, sTGCs will be closely related to the main analysis of this thesis.

3.2.4 The Trigger System

The proton-proton bunch crossing rate is on average 40 MHz in the ATLAS detector [36]. With 140 million channels, an event takes up ~ 1.5 MB of memory. In

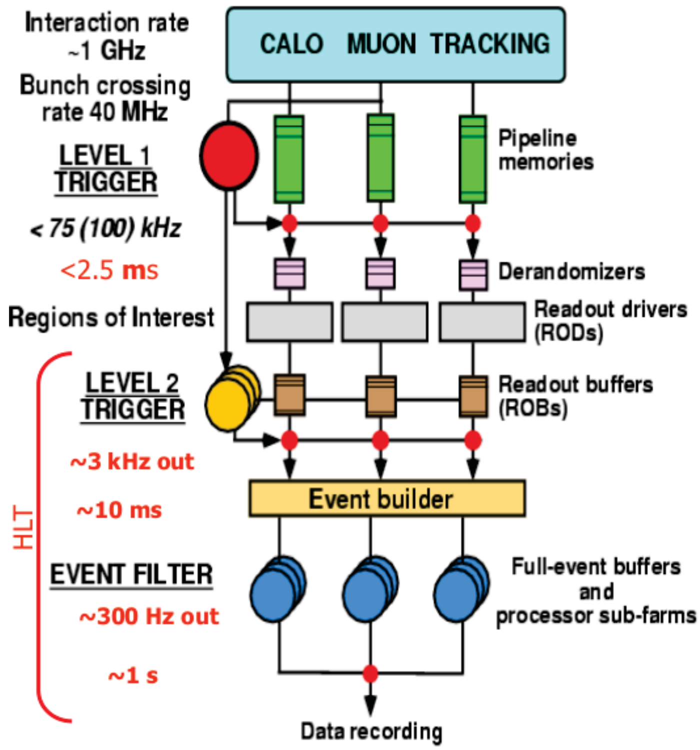

Figure 3.7: A Schematic of the ATLAS Trigger System. Event rate is shown at different levels of the triggering process.

total, this would represent a data storage rate of 1 PB/s if every event was stored without an online selection. Realistically, the ATLAS detector has a bandwidth of 450 MB/s, which means that the storage rate has to be reduced from 40 MHz to about 300 Hz (a 99.9995% reduction). This would generate 4 PB/year of data for offline analysis. The system that handles selecting relevant events online (as the data is being recorded) is called the trigger system (pictured at figure 3.7). It uses information from different detectors, along with software algorithms and dedicated hardware components, to search for specific particle signatures that are considered to be interesting, such as electrons, muons, τ-leptons, photons, B-meson and jets, as well as missing transverse energy (for neutrinos).

The trigger system is divided in three different levels: Level 1, High-Level, and Event Filter.

Level 1 trigger (L1):

Basing its selection from a subset of detectors, it searches for electrons, muons, τ-leptons decaying into hadrons, and large missing and total transverse energy (for neutrinos). It uses data (stored in a temporary buffer) from trigger chambers of the MS, as well as reduced-granularity information from all calorimeters to make this selection. The L1 trigger also defines regions of interest in every event by identifying the η and ϕ coordinates of locations where an interesting signature meeting the selection criteria has taken place.Events that pass the selection are fed to the high-level trigger (L2). In total, the L1 trigger makes a decision every 2μs, including the time necessary to transfer the data to L2.

High-level trigger (L2):

The L2 trigger is seeded by the region of interest defined by the L1. It uses all available detector data within the region of interest at full granularity and precision (which represent $\sim 2\%$ of the total event data). With an average processing time of about 40ms, the L2 reduces the trigger rate to approximately 3.5Hz. The events that passed the selection are sent to the event-building system, and are then fed to the Event Filter.

Event Filter (EF):

The final selection, it uses a processing time of the order of 4s to reduce the event rate to roughly 200Hz. Its selection is based on offline analysis procedures.

3.3 New Small Wheel Upgrade Necessity

Over the next decade, the instantaneous luminosity of the LHC is expected to reach up to 5 times the design value of the luminosity (10^{34}cm^{-2}s^{-1}). This gain in luminosity is necessary to extend the sensitivity to new physics to the multi-TeV range. In parallel with this upgrade, the ATLAS detector will follow an upgrade program of its own in order to cope with the increased rate of collisions. Among these upgrades, the innermost stations of the end-caps of the Muon Spectrometer will be replaced by the New Small Wheels (NSW) (figure 3.8) in 2019-2020 during the LS2 shutdown period. The NSW will provide trigger and tracking capabilities for the first time in this region of the detector (figure 3.9). It has been designed to cope with the high background rates expected at luminosities between $2-7\times10^{34}$cm^{-2}s^{-1} during Run-3 and high luminosity LHC (HL-LHC). Both NSW will consist of 8 layers of MicroMegas (MM) and small thin gap chambers (sTGC), totalling an active surface of 2500 m^2. Upon completion, it will be the largest system based on micro-pattern gaseous detectors (MM) and wire detectors (sTGC).

3.3.1 sTGC structure

In the NSW, the sTGC planes will be arranged in two quadruplets. For offline track reconstruction purposes, the spatial resolution of each sTGC layer should be about 100μm. For online triggering purposes in the ATLAS detector, the angular resolution of the sTGC quadruplets must be better than 1 mrad [37]. The quadruplets are operated with quenching gas mixture of CO_2-pentane (55%:45% by volume) at a typical high voltage (HV) of 3 kV. The quenching gas is necessary to operate the detector in a high amplification mode, since it prevents the occurrence of

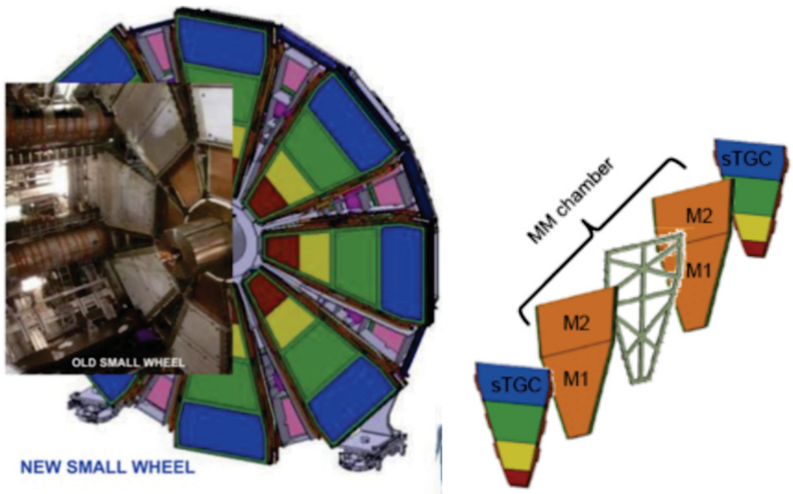

Figure 3.8: Left: Schematic of the 16 sectors of the NSW. A picture of the current Small Wheel is superimposed. Right: Schematic of disposition of the four multilayers of MM and sTGC, along with the support structure. [4]

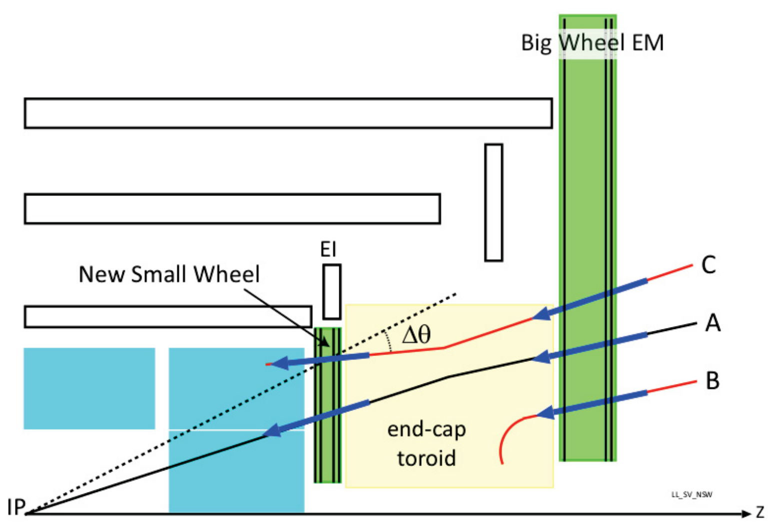

Figure 3.9: Motivations for the implementation of the NSW include rejecting fake muon tracks. The existing Big Muon Wheel accepts tracks A, B and C. The fake tracks (B and C) will be rejected in the trigger by the NSW. [4]

streamers [38].

The precursor of the sTGC, the Thin Gap Chamber (TGC), has been invented in 1983 [38]. Since then, it evolved into its current form, the Small-strip Thin Gap Chamber (sTGC), which is able to provide more precise measurements. A TGC is a multi-wire chamber (figure 3.10) operated in saturated mode. An array of wires held at high voltage (anodes) are sandwiched between two planes held at ground (cathodes). This forms an electric field that draws extra electrons or negative ions to the anode wires with as little lateral motion as possible. The space between the wires and the cathode planes is filled with a specific gas, in our case a gas mixture of CO_2-pentane concentrated at 55vol%:45vol%respectively. This gas mixture is chosen so that any ionizing particle that traverses it will ionize surrounding atoms in the gas. The resulting electrons and ions are accelerated by the electric field, which causes a localized shower of ionization (Townsend avalanche) [39]. This ionization is then collected by the nearest wires, each collecting a charge proportional to the ionization effect of the detected particle. From this, the location of the ionization can be inferred from the location of the wire(s) that recorded the biggest charge collection. By using a quadruplet, an ionizing particle will ionize each of the four gas gaps, which will be picked up by the wires on each layer. This is used to know the trajectory of the ionizing particle traversing the detector.

The basic structure of an sTGC layer is shown in figure 3.11.Tungsten wires of 50μm laid 1.8 mm apart in groups of 20 and held at a 3 kV potential are located between two cathode planes respectively 1.4 mm above and below the wire plane. Perpendicular to the wires and behind the cathode planes on one side of the anode plane, copper strips are laid 3.2 mm apart. This pitch is much smaller than the strip pitch of the current ATLAS TGC, which varied between 150 mm and 490

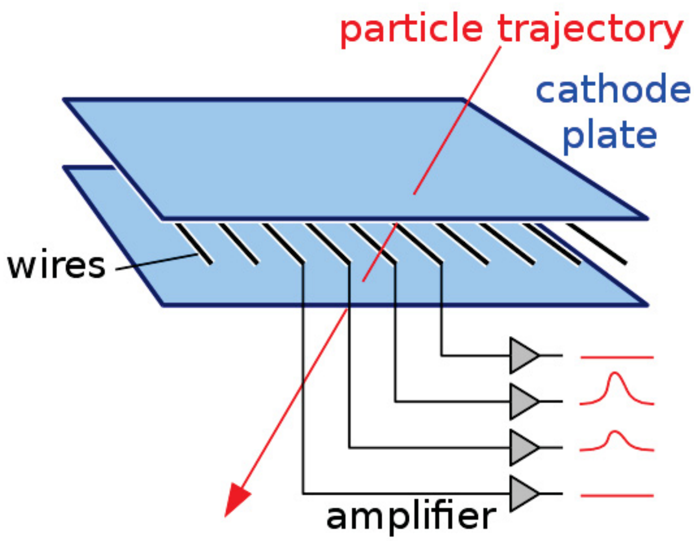

Figure 3.10: Schematic of a multi-wire chamber.

mm (hence the name 'small-strip TGC'). These strips provide the most precise coordinate measurement in the sTGC. Finally, on the other side of the anode plane are copper pads used for fast trigger purposes. Each sTGC quadruplet consists of four pad-wire-strip layers like the one pictured in figure 3.11. We will use the word **sector** to designate a layer and plane combination in the sTGC (e.g., L2S is a sector for the second layer of strips). Since the sTGCs will be assembled in a wheel, the sTGC quadruplets will all have trapezoidal shapes, with surface areas between 1 and 2 m^2 (see figure 3.12).

3.3.2 Canadian sTGC Program

The construction of the sTGC sectors for the NSW is handled by Canada, Chile, China, Israel and Russia (figure 3.12). For the Canadian parts of the sTGC, which represent a fourth of the sTGC on the NSW, construction begins at TRIUMF in Vancouver. Bare FR4 printed circuit boards with etched copper strips and pads

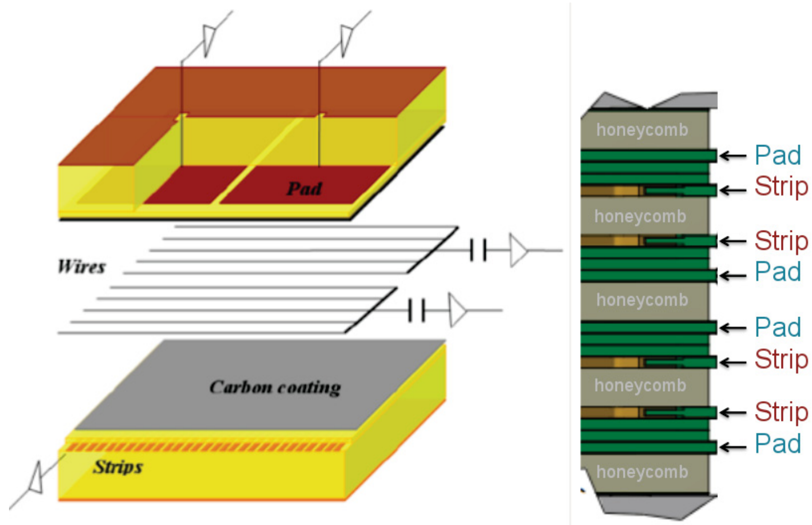

Figure 3.11: Schematics of the basic structure of an sTGC (left) and quadruplet structure (right). [40]

(supplied by Trilabs) are coated with graphite at TRIUMF and various acceptance tests are executed. These planes are then shipped to Carleton University, in Ontario, where they are wired as shown in figure 3.11 and assembled into quadruplet modules (4 gas gaps between planes). They are then shipped to McGill University in Montreal, which does the characterization of the quadruplets and the quality control. In particular, the goal is to measure the hit efficiency and spatial resolution of the sTGC planes. This measurement relies heavily on the ability to properly track the passage of particles in the detector. The tracking aspect will be discussed in chapter 4 of this thesis. Quadruplets which meet the tolerance requirements are then shipped to CERN for assembly into the NSW. The whole Canadian production chain is pictured at figure 3.13.

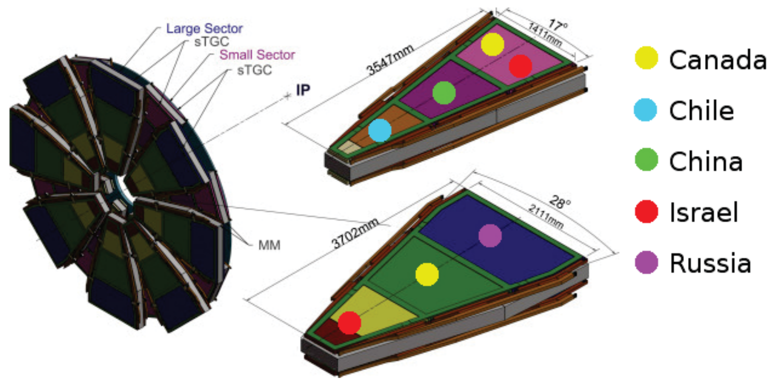

Figure 3.12: Schematic of the small and large sTGC sectors and the corresponding production sites. [37]

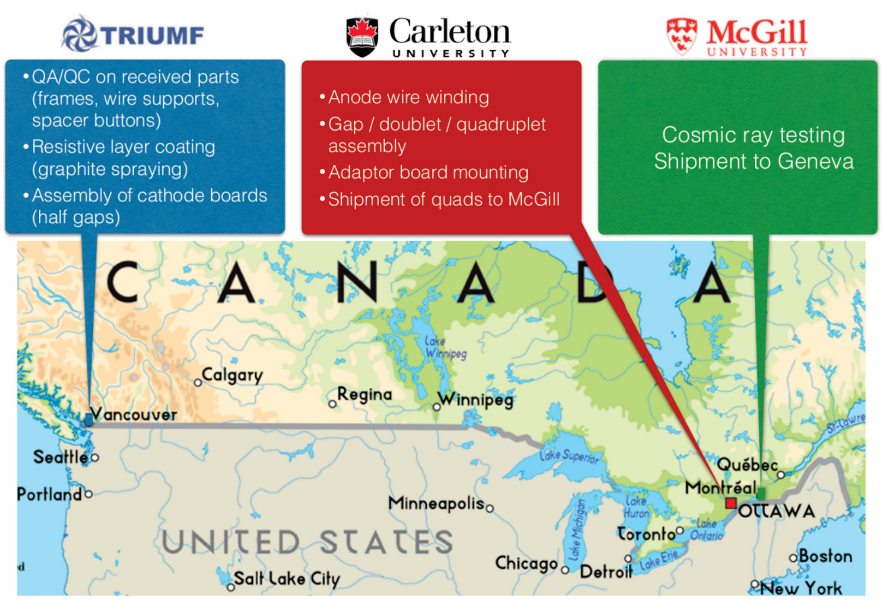

Figure 3.13: The Canadian sTGC quadruplet production and testing chain

3.3.3 40×60cm^2 sTGC Prototype

While the trapezoidal sTGC quadruplets are being constructed, a rectangular 40×60cm^2 cm^2 sTGC detector (figure 3.14) is being used in the McGill lab. This prototype is useful for the McGill staff to gain experience with their system and prepare analysis algorithms for the data recorded by the sTGC detector. It has been designed by the Weizmann Institute Group and built in Israel by the Canadian sTGC group (TRIUMF and Carleton U). Along with the readout electronics, this prototype has been tested at Fermilab during a beam test [37]. Just like the trapezoidal detectors, the 40×60cm^2 detector uses cosmic rays as a muon source to ionize the quenching gas mixture of pentane and CO_2 flowing between its cathode boards. The only difference lies in the shape of the detectors: the trapezoidal sTGCs are twice as long and large as the 40×60cm^2 detector. Thus, the 40×60cm^2 detector records approximately a quarter of the events recorded by its bigger counterparts. Because the prototype is rectangular, the geometry of its wires is also much simpler.

Readout Electronics of sTGC Prototype

An application-specific integrated circuit (ASIC) known as the VMM1 chip [41] has been developed in 2012 to read out pad, strip and wire information from sTGC detectors. It is a prototype of the final electronics that will be used in the ATLAS NSW (see figure 3.15). The VMM1 is used in conjunction with a Jack card that handles the digitization of the analog information read by the VMM1 from the sTGC quadruplet. The VMM1 ASIC has been tested at the Fermilab and CERN beam tests to read out pads and strips from the sTGC [37]. Since then, an up-

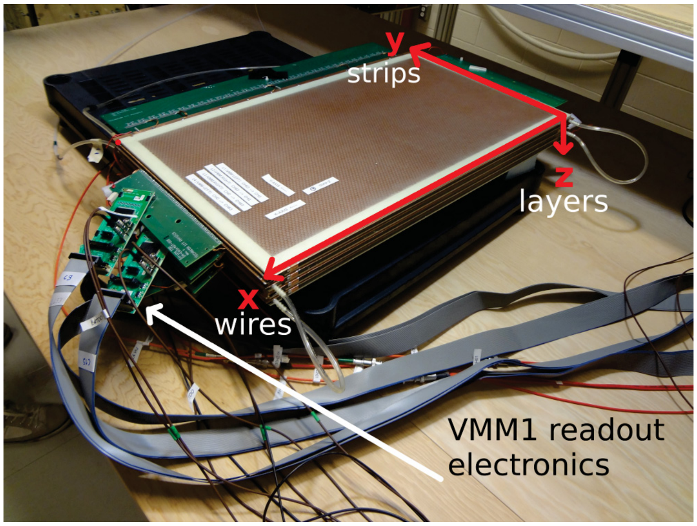

Figure 3.14: The $40 \times 60\text{cm}^2$ sTGC prototype, with the analysis' axis annotated.

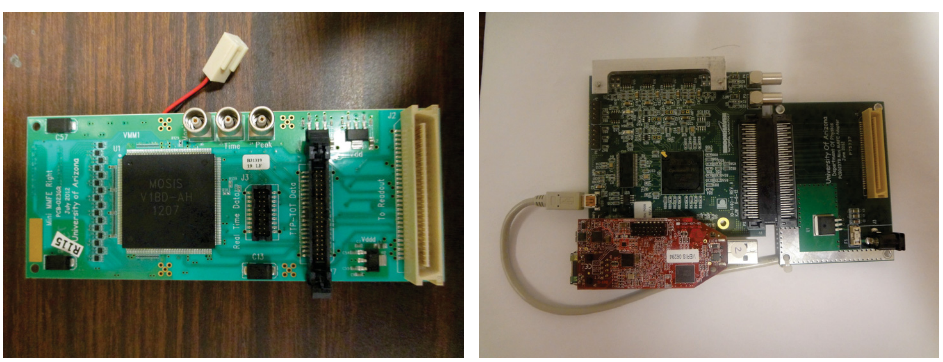

Figure 3.15: The VMM1 ASIC (left) and its Jack card (right). The Jack card is used to configure the VMM1 during operations, and digitization of the VMM1 data

dated version of the VMM1, known as VMM3, has been developed and contains all the necessary features for its implementation in the ATLAS NSW. Among other things, it removes the need to use a Jack card, since the VMM3 can handle the data digitization on its own. However, since the VMM3 ASIC has not yet been released, the data presented in this thesis has been recorded with VMM1.

The amplitude of the analog signal read by the ASIC is designed to be proportional to the input charge for a given channel. The ASIC readout is zero suppressed, which means that only channels with peak signals above a predefined threshold are read and digitized. The VMM1 contains a shaper circuit that outputs the analog peak value of the signal for each channels. It is possible to configure the VMM1 to also read the signal amplitude for channels adjacent to a channel above threshold (known as neighbor-triggering). Using neighbor-triggering and the internal calibration system of the VMM1, it is possible to record the baseline of each readout channel in the sTGC. This is done by sending a test pulse on a single readout channel and recording the peak values of the neighbor channels (which constitute a channel-by-channel baseline) [42]. It is this baseline that is used as the predefined threshold for the ASIC readout, and sits around 180 mV with a variation of $\pm 3\%$ for each channels around this average value.

It is possible to estimate the precise position (x, y) of a charged particle traversing the sTGC gas volume on each of the four detector planes in the sTGC quadruplet. To determine the centroid of the charge deposition on the strips axis, a Gaussian is fitted over the measured charge of adjacent readout strips (known as a strip-cluster). This is in fact a necessary step to reconstruct tracks of particles inside the detector, as will be discussed in section 4.4.2.

40×60cm^2 sTGC Data Acquisition

The VMM1 data acquisition (picture at figure 3.16) relies on the VMM1 ASIC, the Jack card and NIM logic unit connected to the scintillators' PMTs. It begins with a pulse in the sTGC quadruplet, for example on the strips axis of layer 2 (L2S). The instantaneous charge deposition on each channel (if there is one) is read as a function of time, and forms as Gaussian shape. Let's pretend channel #10 received a charge deposition for the sake of the example. If neighbor triggering is enabled for the run and channel #10 recorded an instantaneous charge deposition above threshold, the VMM1 starts reading channel #9 and #11 (neighbors of #10), regardless of their instantaneous deposited charge. As the charge is being deposited on each channels, the peak detector ramps up simultaneously, but hangs on to the maximum value of instantaneous deposited charge for each channel. This value is the channel Peak Detector Output (PDO). When a maximum PDO value above threshold has been found, a flag on the VMM1 is set to high. At the same time, as soon as the instantaneous deposited charge starts going down, an analog time detector counts the time between the peak of a channel and the TACstop signal. This time value is defined as the time over threshold, or Time detector Output (TDO). So far, all of this is happening within the sTGC detector and the VMM1.

The TACstop signal comes from the external trigger. It is set to happen with a delay of 3μs after the detection of scintillation in the scintillators by the PMTs to give time to the VMM1 to read the different sectors of the VMM1. This delay is known as the "trigger timeout window" and is a parameter that can be modified upon starting an sTGC data run. When the VMM1 receives the TACstop signal, it stops reading the content of the sTGC momentarily to either send the signal to the Jack card to start digitizing the data (only if the analog "flag" is set to high), or

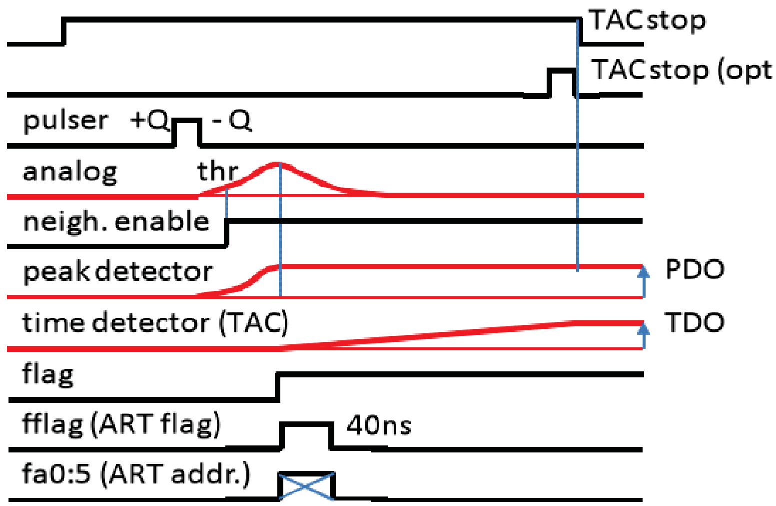

Figure 3.16: A typical timing diagram for VMM1 data acquisition [41].

resets its memory without recording the event (otherwise).

3.4 McGill sTGC Test Bench

The McGill sTGC Test Bench consists of a $10.2\text{m} \times 5\text{m} \times 2.5\text{m}$ room on the second floor of the Ernest Rutherford building on the McGill University Campus. The lab is divided in 4 sections: the gas system, the hodoscope, the loading station, the slow control computer. All four sections of the lab can be seen in figure 3.17.

3.4.1 Gas System

To operate sTGC quadruplets, in addition to providing high voltage necessary to operate the sTGC quadruplets, a continuous flow of pure gaseous CO_2 or gaseous CO_2:pentane mixture (respectively 55vol%:45vol%) must be provided. For this task, a gas system was custom designed for the sTGC testing facility (figure 3.18).

In order to achieve a concentration of 55vol%:45vol% for the CO_2:pentane

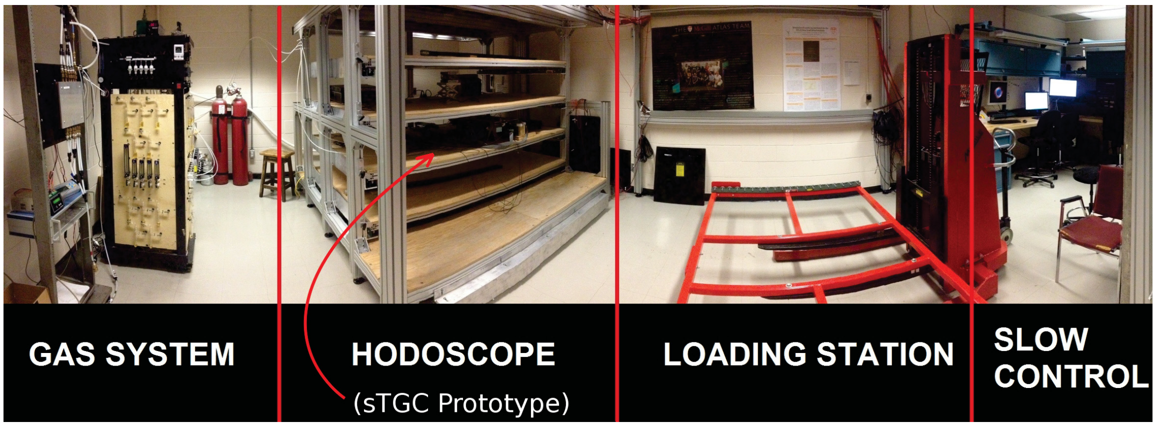

Figure 3.17: The McGill sTGC Test Bench.

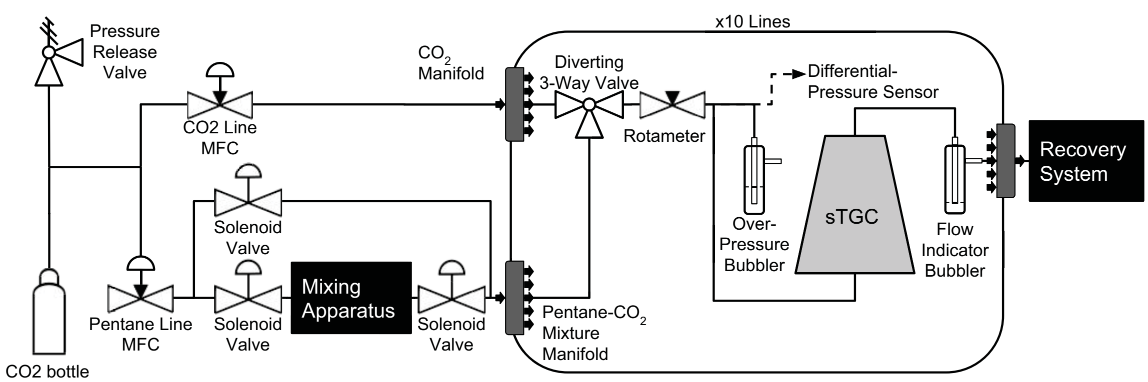

Figure 3.18: Diagram of the gas system. Gas flows from left to right. Pure gaseous CO_2 flows on the CO_2 line, whereas the CO_2:pentane mix flows on the pentane line. [5]

mix, a dedicated mixing apparatus was integrated to the gas system design (figure 3.19). It consists of two main parts: a Peltier thermoelectric cooler (TEC) and a hermetic liquid mixing vessel. The mixing apparatus takes as an input pure CO_2 gas and liquid pentane, and outputs a gaseous mix at the desired concentration. First, a saturated CO_2:pentane mixture is created at room temperature (~ 20°C), which is at higher concentration than desired to use in the sTGC quadruplet. Then, the TEC cools down the gaseous gas mixture, of which a part condenses back into the mixing vessel due to gravity. The mixing apparatus was characterized [5] (figure 3.20), and a cooling temperature of 14.5°C is used to produce the correct CO_2:pentane mix.

The development and characterization of this gas system has been documented [5], as well as its safety features for operation.

3.4.2 Hodoscope and scintillators

The hodoscope is $2.6\text{m}\times2.6\text{m}\times2.2\text{m}$ (height) structure with an aluminum frame on which 4 equally spaced drawers (wood sheets) can hold sTGC quadruplets. At the top and bottom of the structure are 2.5 cm thick scintillator sheets read out by photomultiplier tubes (PMTs) which provide the trigger signal for the sTGC quadruplets. There are a total of 8 scintillators in the hodoscope, 4 at the top and 4 at the bottom. The PMTs are connected to a Nuclear Instrumentation Module (NIM) crate which provides the trigger logic. For an event to be potentially recorded, there needs to be a coincidence within 100ns between a top and a bottom scintillator. If this is the case, data coming from the sTGC is read, and if there is any channel above threshold, the data is kept (see section 4.2). The detection process is illustrated in figure 3.21.

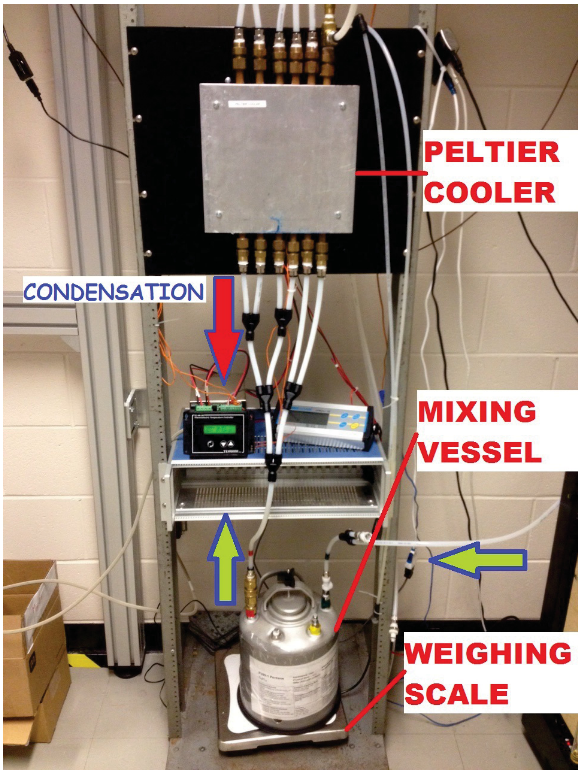

Figure 3.19: The gas system's mixing apparatus

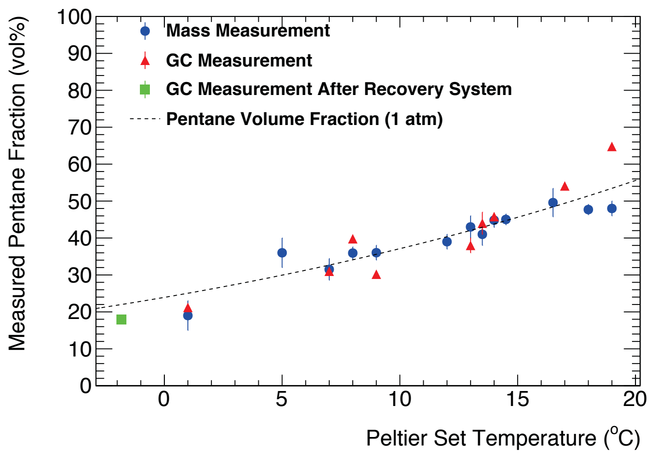

Figure 3.20: The pentane concentration of the CO_2:pentane gas mixture produced by the mixing apparatus for different set temperatures. Each measurement was done independently. Multiple measurements for each Peltier set point are combined. The pentane concentration is measured using two different methods: a mass measurement (blue points) and a gas chromatography measurement (red points).

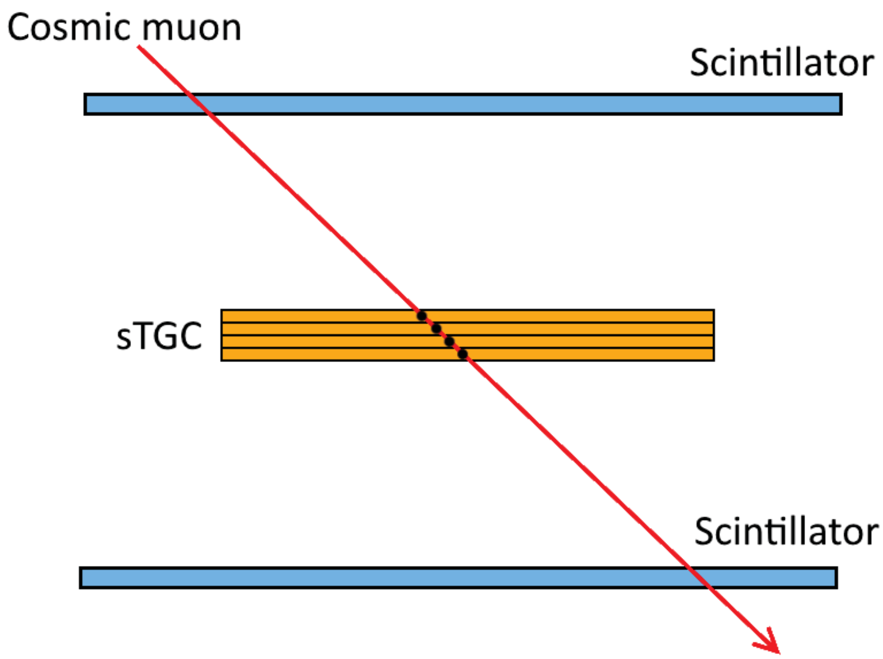

Figure 3.21: A cosmic ray muon traversing the hodoscope leaves a charge cluster on different layers of the sTGC quadruplet. The top and bottom scintillators are used as triggers.

3.4.3 Slow Control

To ensure the integrity and safety of the sTGCs and to minimize sources of human error, a slow control and its associated state machine have been developed. These provide automated safety actions, system control and conditions monitoring. The slow control system reads data provided by many sensors integrated in the testing facility, such as pressure, humidity, temperature and combustibility. These sensors are strategically positioned in the gas system to provide insight on the system's performance. The state machine interface (see figure 3.22), programmed using LabVIEW, logs the data and presents plots it in real time to the operator.

Under certain predefined conditions, the sensor values can automatically trigger safety actions, such as bypassing the mixing apparatus (flow pure CO_2

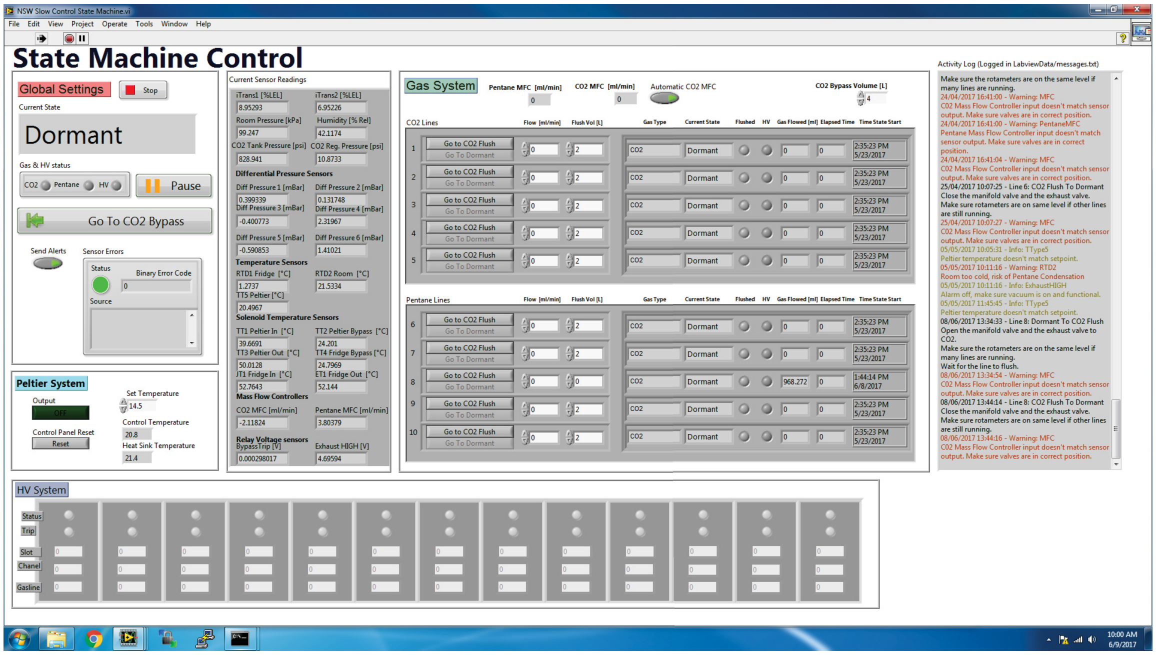

Figure 3.22: A screenshot of the McGill testbench state machine (LabVIEW). The state machine gives the status of every gas line and live data from the gas system sensors. There is also an activity log on the right side that recent activity and any error that occurred.

in the sTGC quadruplet) and turning off the high voltage. These safety features enable operators to monitor the state of experiments overnight without the need to be physically in the lab at all times to monitor the experiment. An alarm system has also been set to notify operators via email and/or SMS when a warning or error condition is raised. However, the slow control system can only be controlled from the testing facility.

Slow Control Monitoring

An online monitoring tool has been developed to display as accurately as possible the state of the gas system for operators not physically in the lab. A web page on McGill's Physics Department[2] is updated hourly by a ROOT script to show data

[2] http://www.hep.physics.mcgill.ca/~legerf/SCATool/

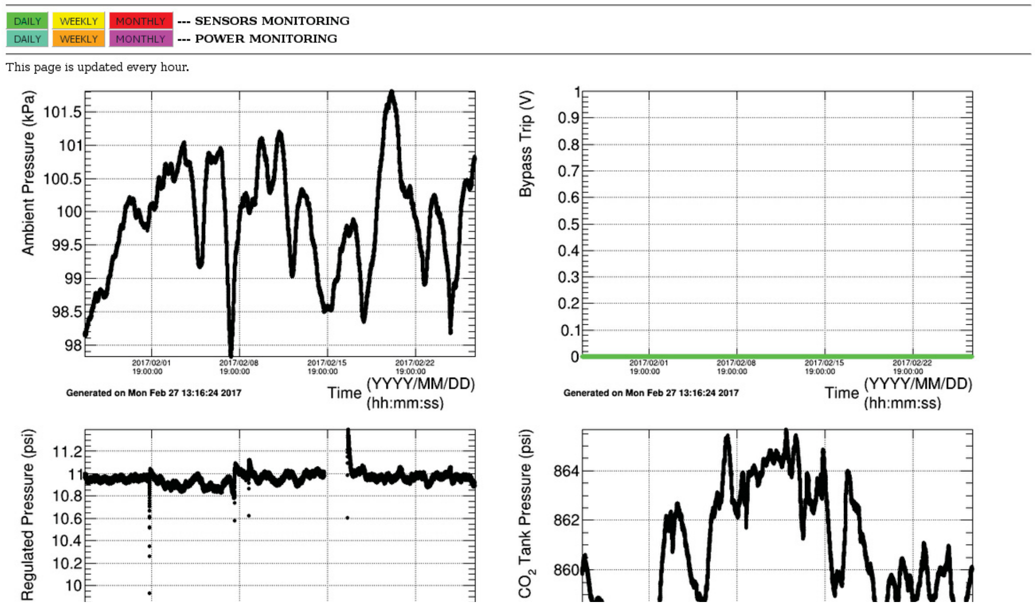

Figure 3.23: The Slow Control Monitoring Tool. The web page is available online, so the lab sensors can be monitored even if no operator is physically present.

recorded by the slow control's sensors (figure 3.23). The Slow Control Analysis Tool (SCATool) reads offline data logged by the state machine every hour and produces plots for every sensor and the high voltage that show data of the last 24 hours, the last 7 days, and the last 30 days. It also shows an error message when data is not being logged by the state machine.

In addition to showing sensor data, the SCATool takes a screenshot every 15 minutes of the LabVIEW state machine and updates it on the monitoring web page (see figure 3.22.). This screenshot alone is enough to know the current state of the whole gas system and high voltage system:

- The status of each gas line is shown (what gas is is flowing, at what rate, for how long)
- The last data recorded by every gas system sensors is shown

- The status of the HV system is shown
- An activity log shows the most recent activity (with time stamps), along with any warning or error that occurred.

To summarize, the McGill sTGC Testing facility currently uses a $40 \times 60\text{cm}^2$ prototype quadruplet along with a custom-built gas system to deliver a CO_2-pentane mixture in preparation for the arrival of the modules that will be implemented in the ATLAS NSW. The next chapter will cover how the data recorded from the $40 \times 60\text{cm}^2$ sTGC detector is used to reconstruct cosmic ray events.

4

Analysis

In this section, we will cover how data recorded from the sTGC detector is used to perform a multi-track analysis. The goal of this analysis is to divide the recorded events in different categories. The analysis requires precise position measurements and uses data from the sTGC strips only (though data from wires and pads is readily available). This analysis is different from the main McGill Testbench analysis that is used to characterize the sTGC quadruplets. Indeed, instead of characterizing the detector, the analysis discussed here characterizes the events recorded by this detector.

4.1 Definitions

Before discussing the analysis, here are some definitions. The following are illustrated in figure 4.1. A charge deposition over a wire, strip or pad channel within a quadruplet layer will be referred to as a **hit**. A contiguous string of hits within a single layer will be referred to as a **cluster**. A Gaussian fit can be made over a cluster to determine its centroid, which is inferred to be the location where the particle crossed a specific layer in the sTGC detector. The width of this Gaussian fit is used as the uncertainty of the position of the cluster on the strips' axis. Finally, a linear fit made over the centroid positions of clusters reconstructed on different layers will be referred to as a **track**. A track is required to contain 3 clusters or more, since fitting a linear equation from two data points will always result in an artificial "perfect" fit from which we cannot learn much. An **event** is all the detector data read out as a result of an individual trigger, and hence everything that happened in the detector within the timeout window. Empty events are discarded and not stored in datasets. Finally, we define the x, y and z axis as they are shown in figure 3.14.

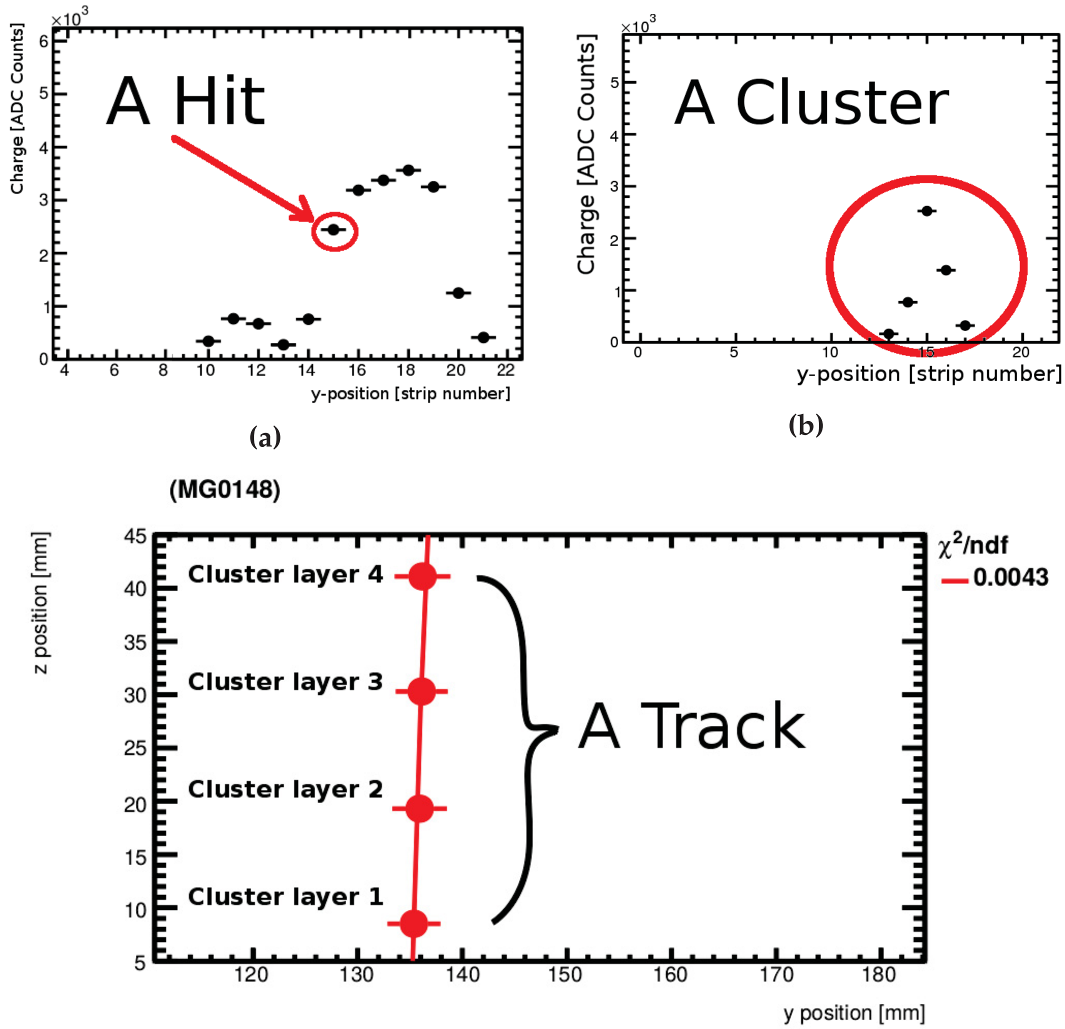

(a) (b)

(c)

Figure 4.1: A hit on a strip channel is shown in figure 4.1a. A contiguous string of hits forms a cluster, illustrated in figure 4.1b. An event is pictured in figure 4.1c, where we can also see a linear fit between different clusters, which we refer to as a track.

4.2 Data format

When the sTGC detector observes the passage of a particle (primarily cosmic muons), channels with data above threshold are read and recorded. This data is converted from analog to a digital format by the VMM1 and jack cards' front-end. This digital format is hexadecimal, and is presented in 32-hex "data words". A typical data word for a channel would look like this:

```
0007aa24004c4e4200000000ee1bb3cc
10.0.0.19fafafafa
```

The first 8 bytes of the first data word contain the trigger number. This number relates to how many times the hodoscope's scintillators observed a top-bottom coincidence, and is always greater than or equal to the number of recorded events. The last 8 bytes contain the channel number as well as peak detector output (PDO) and time detector output (TDO) values. The PDO is a measurement in arbitrary units (Analog to Digital Conversion, ADC) that is proportional to the charge that was deposited on a specific channel during an event. The TDO is the elapsed time between the detection of a charge deposition peak and an external trigger (see figure 3.16).

The 004c4e4200000000 in the middle is a constant header used to ensure data is not corrupted. Finally, the second data word gives the IP address of the sector that recorded the data, followed by "fafafafa", which signifies the end of the recorded event data for this sector.

After data taking is done, a ROOT Tree is built from the offline data. The format of the ROOT Tree is shown in table 4.1).

TTree entry	Description
RunNumber	The run number is stored for each event as a string
EventNumber	Each entry corresponds to one event
IPaddress	Vector of all IP addresses read in this event
Channel	Vector of channels numbers that recorded charge deposition during event
PDOADCcount	Vector of vectors of PDO values, one inner vector per IP in the event
TDOADCcount	Vector of vectors of TDO values, one inner vector per IP in the event
DataQuality flags	Vector of vectors of data quality flags. One inner vector per IP in the event.

Table 4.1: Structure of ROOT Tree containing sTGC data

4.3 Data preparation and cleaning

To be able to manipulate and analyze the sTGC data, it has to be well organized. From the ROOT tree, for every event, we find every channel that recorded a charge deposit above threshold (referred to as a hit, see figure 4.1). Then, from all contiguous hits on a same layer, we form a cluster. In accomplishing this step, there is a possibility that contiguous hits form two overlapping clusters, or that dead channels result in non-contiguous groupings. To solve these potential issues, an intermediate step (discussed later) looks at such “problematic” clusters and either splits overlapping clusters into two different clusters, or reconnects clusters containing a dead channel by extrapolating the missing PDO value. Finally, by fitting a linear trajectory over clusters located on different layers in the detector, we form a track. There are 4 crucial steps between forming clusters and getting a fit: several cuts and manipulations are applied to make sure the data is of good quality. Firstly, a bad channel extrapolation is done, then pre-selection cuts, then double maxima cluster splitting, and finally cluster cuts. Figure 4.2 shows a cutflow, where we can see how many events get through each cut. The cuts are detailed below. Since any cut in data can introduce bias, the cuts used in the analysis have been designed to introduce as little bias as possible. What they remove are events or clusters that

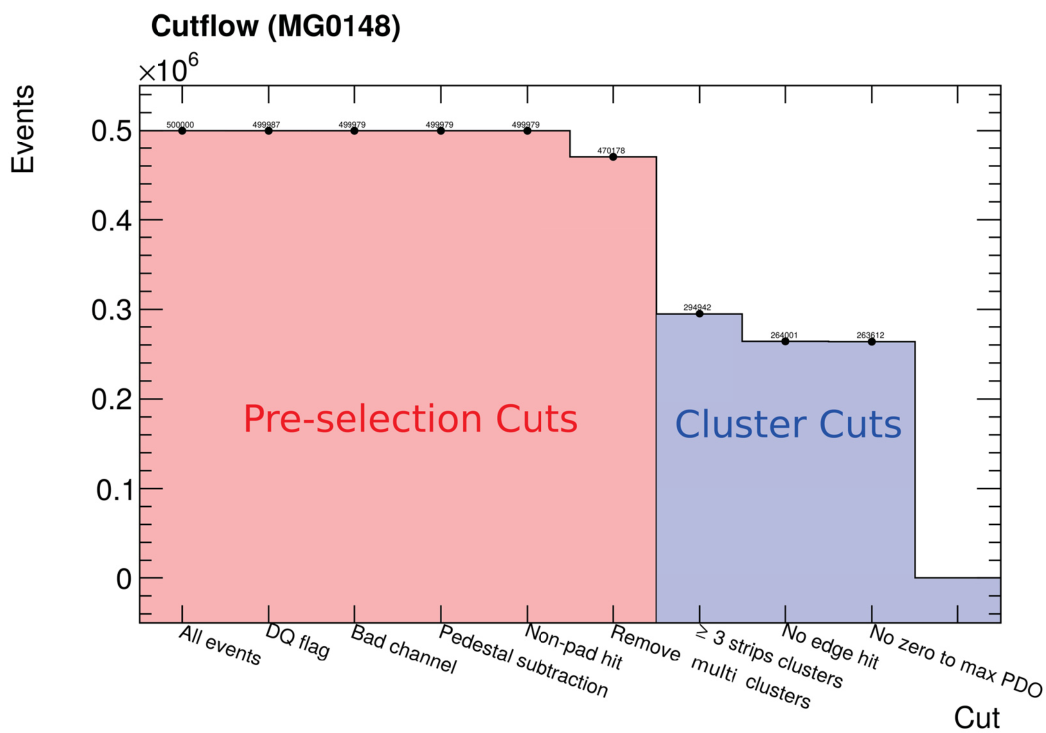

Figure 4.2: The cutflow through which each analyzed event must pass. If an event fails a cluster cut, it is because the event empty after the cluster cut.

cannot be reconstructed by our algorithm due to physical limitations of the detector (e.g. edge effects, missing channels or regions, etc.). They mostly focus on giving data over which we can make Gaussian fits (clusters) and linear fits (tracks). In short, possible bias is minimized by cutting only on data quality and not cluster "kinematics", for example.

Note that these cuts will also be performed as part of the event pre-selection in the single-track efficiency studies for the sTGC module acceptance tests.

4.3.1 Bad channel extrapolation (data preparation)

While the purpose of the nominal sTGC module tests is to identify badly performing regions of the modules, this is not the goal of this study. Our current test uses pre-production electronics and a prototype module with known issues (for example, dead channels on certain layers). These issues are mostly due to faulty electronics, rather than the detector itself. Discarding data that contains some of these issues would result in a lack of statistics. The work-around used in this analysis is instead to simply "ignore" badly behaving channels in order to keep as much data as possible. The most common manifestations of an "abnormal" channel behavior are either when a channel keeps recording data very close to its threshold value, or records almost no events at all. This can be seen for a specific run in the strips sector in figure 4.3. The specific selection criteria are the following: For a channel to be labelled as a "bad channel", it must have inefficiencies. For example:

- The channel has $> 99\%$ of its hits at a PDO value of less than 1500 (compared to an average threshold value of roughly 900)
- The channel does not record data for a certain range of PDO, when compared to other channels of the same layer
- The channel records less than 100 hits during a complete run

In all cases, the bad channel manifests itself similarly in the analysis . It creates a hole in an otherwise contiguous string of hits, which effectively splits a cluster in two (see figure 4.4). The adopted solution is to set the PDO value for the bad channel to be equal to the mean of the PDO of its neighbors (if the bad channel lacks 2 neighbor hits, it is simply ignored). The resulting PDO value itself is of

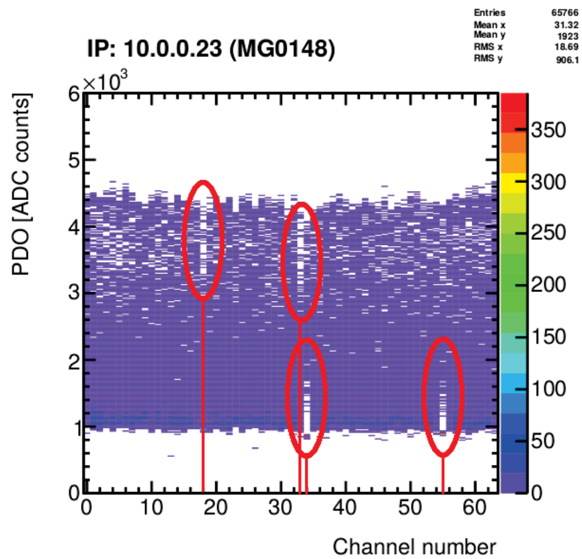

Figure 4.3: Identifications of bad channels in the strip sector of a sTGC $40 \times 60\text{cm}^2$ prototype. On this specific strip layer, channels 18, 33, 34 and 55 present inefficiencies. In the analysis, they are flagged as bad channels and their PDO value will not be included in the Gaussian fit of the strip cluster.

no importance, as the goal is simply to bridge the cluster into a single cluster. An extremely large uncertainty is set to the PDO value of the bad channel (100,000). Thus, if the analysis is configured to ignore PDO uncertainty, bad channel extrapolation cannot be used and is replaced by the bad channel selection cut instead (see 4.3.1). Because of the high PDO uncertainty on the bad channel, this channel is not included in the cluster Gaussian fit later in the analysis, and therefore makes the cluster whole without having a negative impact on the position measurement of the particle through the detector. This step is not a cut.

4.3.2 Pre-selection Cuts

Before events are reconstructed into clusters and tracks, a quick analysis is made at the hit level for each event to ensure its data is of good quality and worth ana-

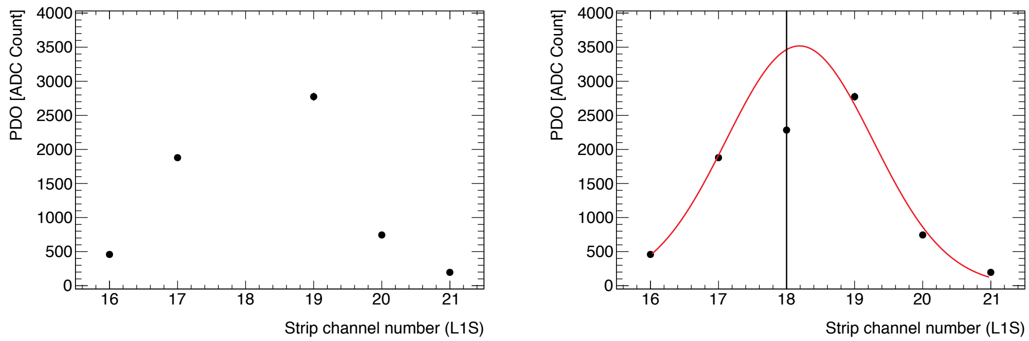

(a) (b)

Figure 4.4: An illustration of a strip cluster before and after an extrapolation of a bad channel. In figure 4.4a, the strip cluster is split in two because of a missing hit on channel 18. Channel 18 is known to be a bad channel for this run (see figure 4.3), so a PDO value (with immense uncertainty) is included before the clustering is done (see 4.4b). The bad channel has little to no effect on the Gaussian fit of the cluster, but is necessary to form a contiguous string of hits.

Cut	Cut Type
Data Quality (DQ)	Event
Bad Channel	Layer
Pedestal Subtraction	Hit
Non-pad Hit	Event
Remove multi clusters	Event

Table 4.2: Pre-selection cuts and the level at which they are applied in data

lyzing deeper. The available pre-selection cuts are the following: DQ flag cut, bad channel cut, pedestal substraction cut, and non-pad hit cut. These cuts are applied at different levels of the data, see table 4.2 for reference.

Data Quality flag cut

In an event, this cut looks at the data quality (DQ) flag for each layer of the $40 \times 60\text{cm}^2$ sTGC quadruplet. In table 4.1, the DQ flag is equal to the number of time a channel is repeated into the same data word. It is used later in the analysis to flag corrupted data, which would have a channel repeat at least once in a data word. If a layer has a DQ flag with a value > 0, the event is cut from the analysis. As seen in figure 4.2, it is very rare for events to be corrupted in a run. This cut is mostly preventive.

Bad Channel Cut

This is an optional cut that is done only if the bad channel extrapolation is not done earlier in the analysis. If a cluster contains a hit over or next to a bad channel, this cut removes data from that layer in the event. This aims to prevent clusters from being split or incomplete (see figure 4.4a). However, it is not applied in this analysis, since the bad channel extrapolation replaces it for the most part by recuperating most of the clusters with bad channels instead of throwing them away.

Pedestal substraction

As discussed previously in section 3.3.3, a baseline recording is made for each channel in the sTGC every time the electronic configuration is modified. This is called a pedestal measurement. The baseline (or pedestal) is the minimum PDO value for a channel to be recorded. The idea is that if a PDO value is below this baseline, there's a high probability that it is noise, and thus not useful data. It is possible for a channel to give a readout value below its threshold (see low PDO hits in figure 4.3, for example channels 13 and 26), and the objective of this cut is to remove these from the analysis.

In all the PDO plots shown in this thesis (except figure 4.3), the PDO values shown are recorded above threshold. The pedestal substraction cut, like the name implies, subtracts the baseline PDO from each hit's recorded PDO value. If the resulting PDO value is below the baseline, the hit is removed from the analysis.

Non-pad hit

Pads are used for fast trigger purposes in the sTGC [37]. They are not meant to be used for high precision measurement, and cannot be used to characterize the resolution or tracking efficiency of a sTGC. Thus, if an event contains only data on the pads (i.e. no data on wires or strips), it is discarded.

Remove Multi-Clusters Events

Events with more than one cluster on any layers of the detector are removed from the sTGC characterization analysis. This is a cut that will be skipped later in the multi-cluster tracking section of this thesis (see section 4.4), since we will analyze what we will define later as "multi cluster events".

For the sTGC characterization analysis, this cut is in place because it aims at removing events that would be potentially difficult to reconstruct and could introduce uncertainty in the characterization of an sTGC quadruplet. Indeed, since no study had been done on multi cluster events prior to this thesis, and since single cluster events represented a large majority of the total events (see figure 5.2), multi cluster events are left aside. One of the goals of this thesis is to find a proper replacement for this cut since "arbitrarily" throwing out events with extra clusters could lead to artificially high efficiency measurements in the context of characterizing a quadruplet efficiency.

4.3.3 Double maxima splitting

When an event reaches this point in the analysis, contiguous hits are grouped into clusters. It is possible for a cluster to contain 2 peaks (see figure 4.5). This

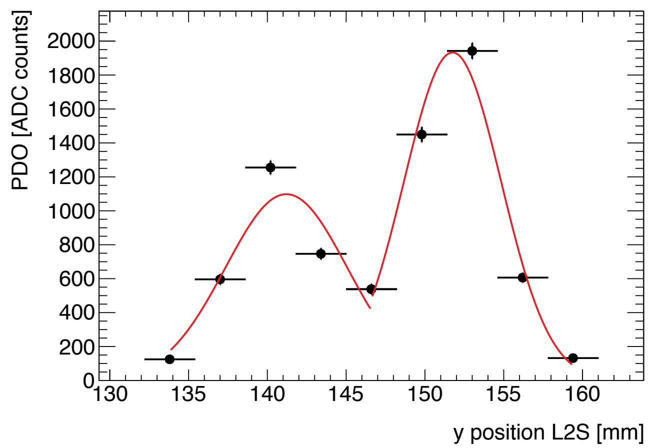

Figure 4.5: If a cluster contains two local maximas, it is separated into two independent clusters to perform a Gaussian fit on each peaks. This is done before doing a track fit.

could happen for example if two independent muons would cross each other in the detector, or travel in parallel trajectories very close to each other. The first step towards analyzing multi-cluster events is to separate the initial cluster into two independent clusters. This is done by following a simple algorithm:

1. Scan the initial cluster from left to right, recording every hit where the sign of the slope changes. These hits are labelled peaks or valleys, depending on if the slope went from positive to negative, or vice versa.

2. Look only at valleys located between two peaks. Keep the PDO value of the peaks with the smallest PDO in memory.

3. If the PDO difference between the smaller peak and the valley is > 300 and is also bigger than 30% of the PDO value of the smaller peak, create a split in the cluster where the valley is located. The hit that was located at the valley is now part of both clusters resulting from the split.

In step 3), the 300 and 30% values are empirical and come from experimentation.

4.3.4 Cluster cuts

The cluster cuts' goal is to remove clusters for which the calculated centroid position cannot be trusted due to the limits of the detector, for example its edges or the size of its strips. The sequence of cluster cuts is the following: small clusters cut, edge clusters cut, and zero to max PDO cut.

Small Clusters Cut

To be able to fit a Gaussian over a cluster, it has to have a minimum of three hits. This is what this cut enforces. The reasoning is that a Gaussian fit needs to have a peak and at least a hit on both sides of that peak to be able to fit reasonably. In the sTGC quadruplet, we ensure that clusters have at least three hits be using neighbor triggering, which records data from channels next to a channel over threshold. With this method of recording, the minimum amount of hits per cluster is 3 (center above threshold, and the two neighbor channels). Even if neighbor triggering is used when recording data, a cluster could still possess less than 3 hits, for example if one of the channels recorded a PDO below the pedestal value. If a cluster in the analysis does not have at least three hits, something went wrong with the recording, and the cluster is completely cut.

Edge Clusters Cut

This cut removes clusters that recorded hits on the first and last channels of an sTGC sector. This is to ensure that no data overflowed on either side of the sector,

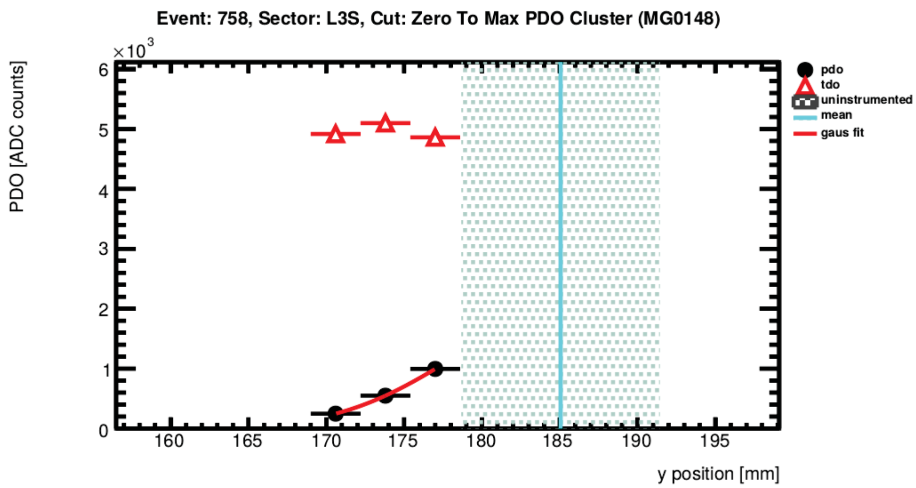

Figure 4.6: An example of a cluster failing the zero to max PDO cut. The fitted cluster position and uncertainty are presented in blue.

which would give an incomplete cluster.

Zero to Max PDO Cut

This cluster cut removes clusters which have their PDO peak on their left or right side. The reason why these are removed is because such clusters give very poor Gaussian fits. Most of the time, clusters that fail this cut have only 3 hits. As seen in figure 4.6, instead of using the peak value of the cluster as the maximum of the Gaussian, the fitter goes to infinity, yielding a big uncertainty on the position of the cluster. To prevent this from interfering with the resolution measurements of the analysis, this cut is applied.

4.4 Characterization of multi cluster events

The main analysis of the McGill sTGC Testbench aims at measuring the hit efficiency and spatial resolution of the sTGC quadruplets, and to do this, it rejects any event with more than one cluster on any layer of the detector, defined as "multi cluster events" (see figure 4.2). In this section, we will study these rejected events and discuss the algorithm that was developed in order to reconstruct them.

4.4.1 Motivation

Early in this project, in the data runs recorded by the sTGC quadruplet prototype at the McGill sTGC testbench, it was found that on average $\sim 4\%$ recorded cosmic muons produced at least two clusters on one or more layers of the sTGC detector. This seemed to disagree with what was expected from early calculations.

These calculations were the following. The rate of muons with energy above 1GeV at sea level is $\sim 1\text{cm}^{-2}\text{s}^{-1}$ [14]. This energy level is easily detected by the sTGC detector. The $40 \times 60\text{cm}^2$ sTGC detector having a surface area of 2400cm^2, this would translate into an average rate of 40Hz in the quadruplet. This yields an average time of 0.025s between two consecutive muons. The number of muons crossing the detector each second can be modeled by a Poisson distribution, which has a probability $P(k \text{ muons in interval } t) = \frac{\lambda^k}{k!}e^{-\lambda}$, with λ being equal to the average number muons in an interval t.

We have $\lambda = 40\frac{\text{muons}}{\text{s}} \times 3\mu\text{s} = 1.2 \times 10^{-4}$. The time t we choose is 3μs, which is the time delay used for the trigger between observing scintillation in top and bottom PMTs of the hodoscope and the recording of the VMM1's data. In this case, the probability of having two independent muons traverse the sTGC detector in a $t = 3\mu$s interval is the following:

$$
\begin{aligned}
P(k>2;t=3\mu\text{s}) &= 1-(P(k=0)+P(k=1)) \\
&= 1-\left(\frac{\left(1.2\times10^{-4}\right)^{0}e^{-1.2\times10^{-4}}}{0!}+\frac{\left(1.2\times10^{-4}\right)^{1}e^{-1.2\times10^{-4}}}{1!}\right) \\
&= 1-0.999999992 \\
&= 7.1994\times10^{-9}\approx 7.2\times10^{-7}\%
\end{aligned}
\tag{4.1}
$$

Since we observed a proportion of multi cluster events of $\sim 4\%$ in the sTGC quadruplet data, which is 5.56×10^{6} times higher than the initial prediction, this presented an interesting opportunity to study the events removed from the McGill Testbench analysis. The initial hypothesis was that multi cluster events could be the result of δ-rays (see section 2.3). Another hypothesis was that some of the multi cluster events could be the result of fake and/or spurious hits resulting from faulty electronics. In order to study these possibilities, a multi-cluster analysis had to be developed.

A GEANT4 [43] [44] simulation was made to estimate the production rate of δ-rays in the McGill sTGC Testbench[1]. This simulation aimed to recreate the two floors above the testbench in the Rutherford Building, as well as the main ceiling which is made out of concrete. Muons with an energy of 1GeV were aimed at a 1 m thick concrete slab. On average, 2.3% of the muons going through this slab of concrete produced one δ-ray or more. It was also found that muons exited this concrete slab with a mean energy of 584.5MeV, which is sufficient to be detected by the sTGC detector (threshold is ~ 1MeV).

[1]More details about this simulation, such as the parameters and end results, are provided in appendix A

4.4.2 Multi-Cluster Tracking Algorithm

This algorithm is used to do tracking on multi cluster events. It uses information on every strip layer of the sTGC detector, but skips empty layers. A typical end result of the multi-cluster tracking algorithm can be seen in figure 4.7.

It is done in four subsequent steps. The first step is to simply assemble a linear fit in ROOT for every combination of clusters possible, using one on each layer with data. The total number of combinations will be equal to $n_1 * n_2 * n_3 * n_4$, with n_i being the number of clusters on layer $i \in \{1, 2, 3, 4\}$. No χ^2 cut is applied, and as a result this selection is as crude as possible.

The second step is to compare every pair of tracks that share two hits in the sTGC quadruplet and cut the one with the highest χ^2/ndf, which represents the worst fit. The idea behind this cut is that objects travelling in a straight line should cross at most once, hence the maximum number of hits that two different tracks should share is 1.

The third step in this algorithm is to look among all tracks that are left, and pick the pairs that still have a common cluster among them. Tracks from these pairs are re-fit linearly, but excluding this hit. This is to avoid effects like the one seen in figure 4.8, where an inefficiency in a layer created a missing cluster and greatly impacted the fit of one of the tracks by forcing it to use a cluster from the other track. This can happen if the cluster was simply cut by earlier cluster cuts, or if the only cluster on a layer is very large, making its centroid position fall between the tracks. It is important to note that since tracks need three clusters or more to be included in the selection, it is impossible to apply this procedure for tracks that have three hits and share a common cluster. These rare occurrences are currently left as is by the algorithm.

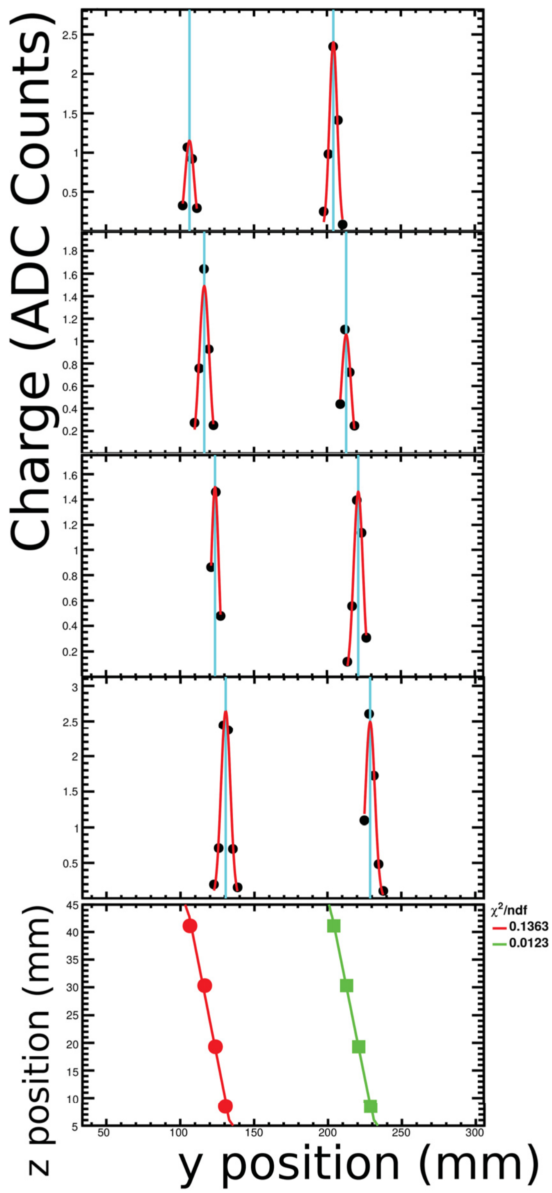

Figure 4.7: Event display of an event reconstructed with the multi-cluster tracking algorithm. The 4 top plots show the hits and clusters from the sTGC, and the bottom plot shows the resulting reconstructed cosmic muon tracks. Note that the two tracks having a similar trajectory could suggest they are related. This would be the case if the event contains a δ-ray.

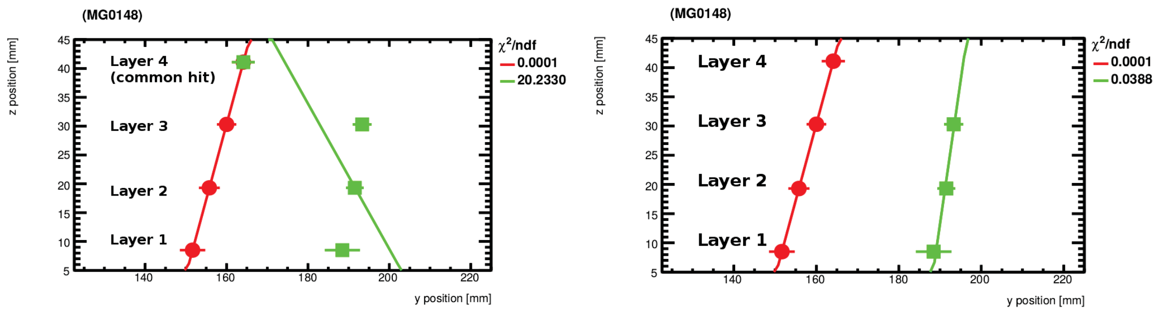

(a) Event reconstruction before re-fit. **(b)** Event reconstruction after re-fit.

Figure 4.8: An event reconstruction before and after the re-fit sequence for a common hit in the multi-tracking algorithm. Re-fitting both tracks by excluding the single cluster on layer 4 greatly increases the quality of the track on the right (green), but will leave the track on the left unchanged.

The fourth and final step is to look is to cut any track with a $\chi^2/\text{ndf} > 10$. This value is empirical and comes from experimentation with the tracking algorithm. As a result, it is possible for an event to possess enough data on different layers to be reconstructed, but ends up being trackless.

By using this multi-cluster tracking algorithm, it is possible to reconstruct cosmic ray events that traversed the $40 \times 60\text{cm}^2$ sTGC quadruplet. The next chapter will discuss how we can discern certain kinds of events based on their reconstruction. In particular, multi-cluster events will be categorized in order to determine whether they could be the result of δ-rays or other phenomena.

5

Results

Using the multi-cluster tracking algorithm discussed in section 4.4.2, it was possible to divide the events recorded by the $40 \times 60\text{cm}^2$ sTGC quadruplet into 7 main categories (see figure 5.1):

- Events with no tracks
- Events with 1 reconstructed track based on 3 clusters, with no additional clusters
- Events with 1 reconstructed track based on 4 clusters, with no additional clusters
- Events with 1 reconstructed track based on 3 clusters, with additional cluster(s)
- Events with 1 reconstructed track based on 4 clusters, with additional cluster(s)
- Events with 2 reconstructed tracks (with or without additional cluster(s))
- Events with 3 or more reconstructed tracks (with or without additional cluster(s))

The last two categories enable the presence of additional clusters not part of the fitted tracks.

If a δ-ray were created from the concrete ceiling of the Rutherford building, both the primary muon and the secondary electron would cross the four layers of the sTGC. Assuming all hits are properly recorded for such an event, it would enter the "event with two tracks" category. A less probable but still possible case is where a δ-ray originates in the sTGC, where the resulting electron would only travel through a subset of the sTGC layers, forming a vertex with the primary muon track. In that case, this event could either be categorized as "event with one track and one or more additional clusters" or "event with two tracks", depending on where in the sTGC the δ-ray is formed. For example, if the δ-ray is formed between the second and third layer in the detector, the secondary electron can be recorded at most on two layers, which is not enough to be fitted linearly in this analysis. In this case, it would be an event with one track and two (or less) layers with additional clusters.

A data run (labelled MG0148) has been taken at the McGill sTGC testbench with the 40×60cm^2 quadruplet prototype and, for 10^6 events, has given the distribution pictured in figure 5.2. The detailed quantities for the pie chart are shown in table 5.1, with an uncertainty corresponding to a normal approximation interval [45]. The initial result is that only 47.9% of the events can be reconstructed with the multi-tracking algorithm, the others lacking data on three different layers or more in the sTGC detector. This is due to the fact many clusters form on the sides of the detector or get polluted by known bad channels. It is worth pointing out that this is a feature of the quality of the prototype electronics and the relatively small size of the 40x60 sTGC. Performance with the "real" sTGCs should

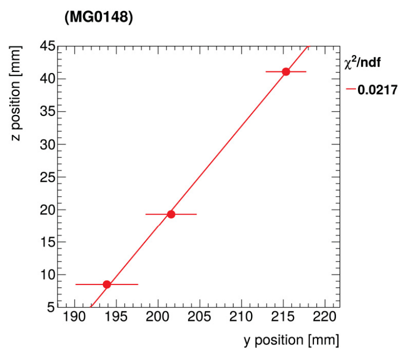

(a) A 1 track event with 3 layers

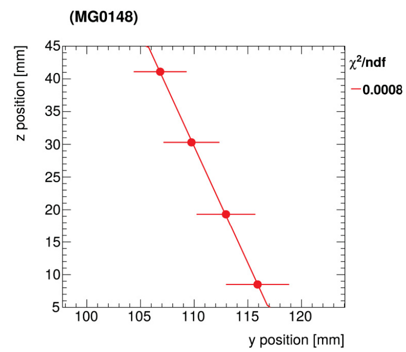

(b) A 1 track event with 4 layers

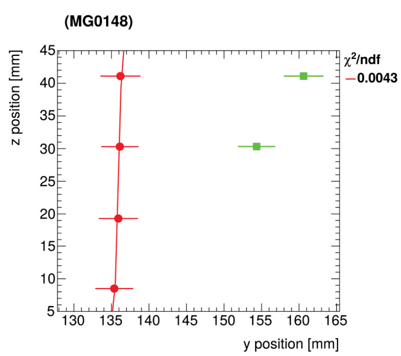

(c) A 1 track (4 layers) event with extra clusters (possible δ-ray formed in the sTGC)

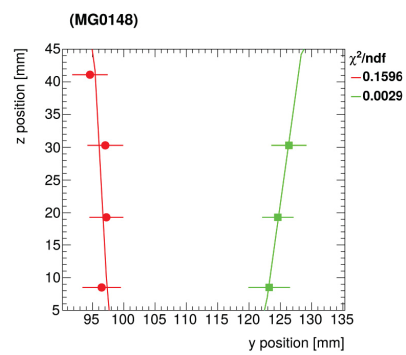

(d) A multi-cluster event with 2 tracks

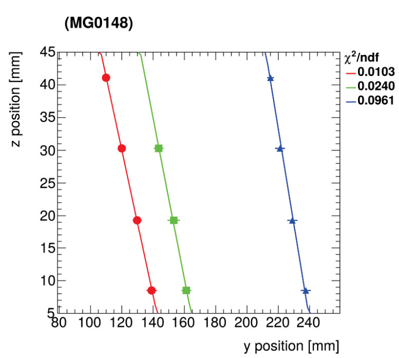

(e) A 3 tracks event

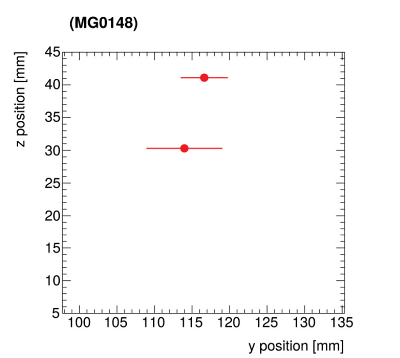

(f) A trackless event

Figure 5.1: Different categories of cosmic ray events, based on their tracking. Note the z-axis is defined to be the direction of the muon flight (from the ceiling to the ground). The first layer of the sTGC quadruplet is at 8.1mm and the fourth layer is at 41.1mm.

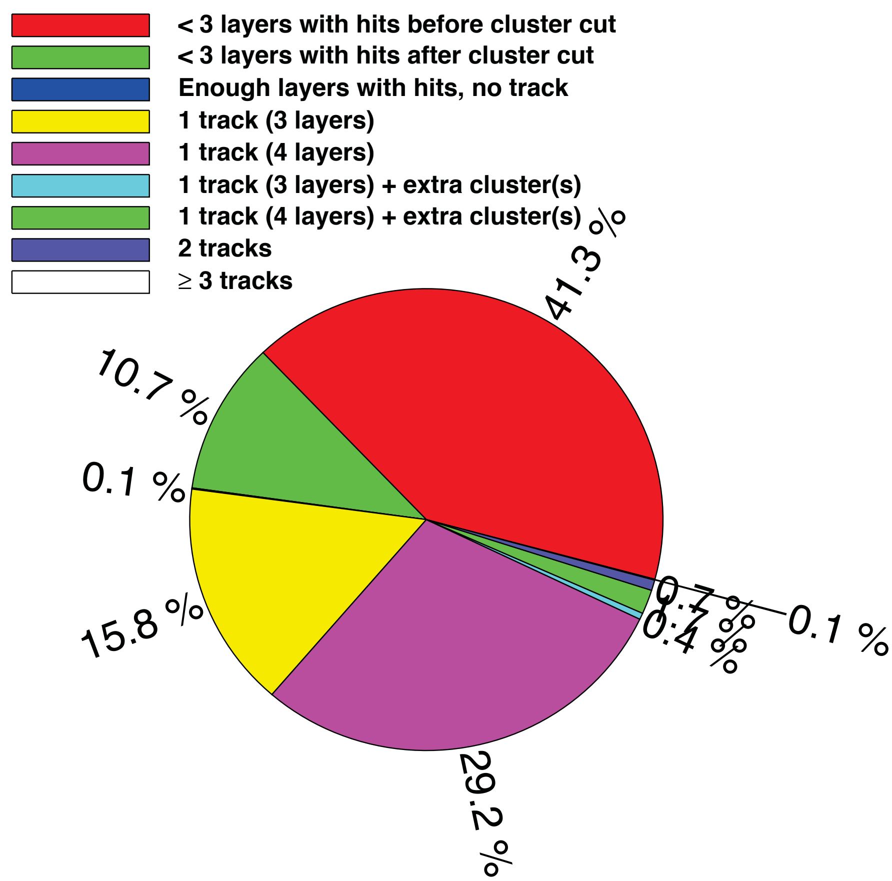

Figure 5.2: Distribution of event types recorded with a $40 \times 60\text{cm}^2$ sTGC quadruplet prototype (run MG0148).

have a much higher rate of successful reconstruction. Figure 5.3 shows the cluster position distribution in the sTGC $40 \times 60\text{cm}^2$ detector. The non-trivial structure in these distributions is indicative of the ”issues” with bad channels and the edge effects in the module.

Of the events containing ≥ 1 track, 93.8% are single track events with a single cluster or less on each layer. These are events that would be used in the standard sTGC characterization analysis to measure the resolution and hit efficiency of the detector. Out of these events, 33.1% are single tracks with 3 layers and no

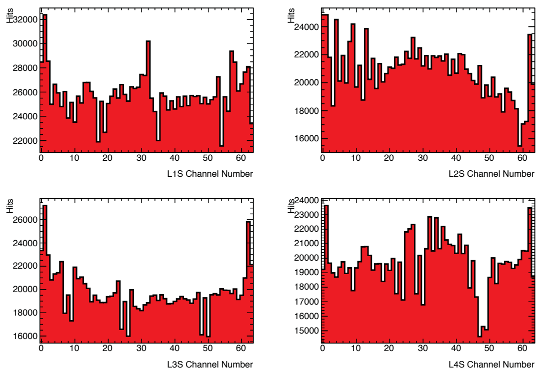

(a) Distribution of the location of recorded hits before pre-selection cuts.

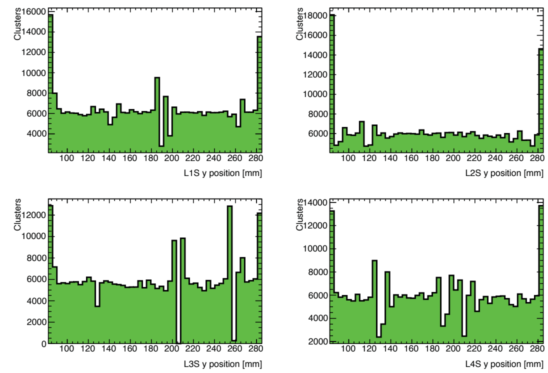

(b) Distribution of cluster positions prior to cluster cuts.

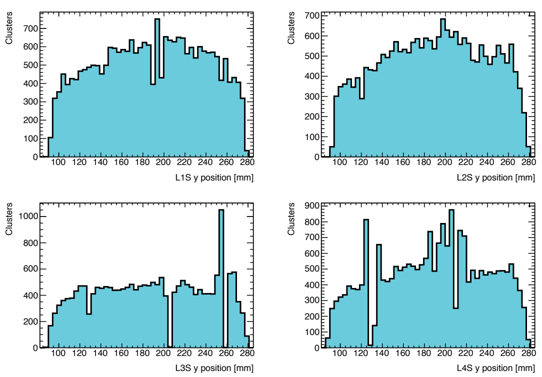

(c) Distribution of the position of clusters part of an event with at least one fitted track.

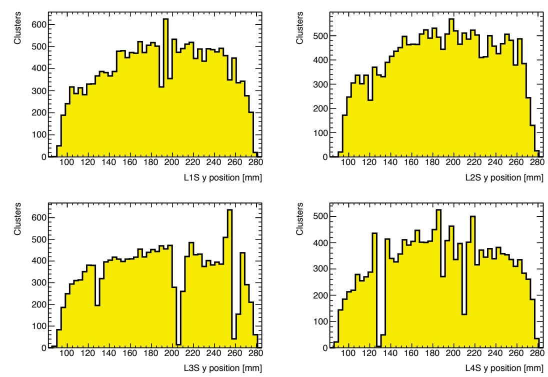

(d) Distribution of the position of clusters on a fitted track.

Figure 5.3: Cluster position distribution in each layer of the sTGC $40 \times 60\text{cm}^2$ detector for run MG0148 for 5×10^5 events. Figure 5.3a shows the "raw" distribution of recorded hits over the strips' channels before any selection cut. It can be seen in 5.3b that a large quantity of clusters have their centroid on the edges of each layer. These edge clusters are not present in 5.3c, since they are removed by a dedicated cluster cut. From both 5.3b and 5.3c, bad channels can be spotted by their lack of clusters. Noisy channels are not present in 5.3d. The bad channels are 18, 33, 34 and 55 for layer 1, 2 and 11 for layer 2, 8 and 25 for layer 3, and 23, 29 and 48 for layer 4.

Table 5.1: Distribution of 5×10^5 events measured by an sTGC prototype (run MG0148).

MG0148	Events	%	Rate (Hz)
<3 layers with hits before cluster cuts	206420	41.28 ± 0.07	55.3 ± 0.1
<3 layers with hits after cluster cuts	53370	10.67 ± 0.04	14.29 ± 0.06
Enough layers with hits, no track	403	0.081 ± 0.004	0.108 ± 0.005
Sub-Total for trackless events	**260193**	**52.03**	**69.7**
1 track (3 layers)	78986	15.80 ± 0.05	21.2 ± 0.8
1 track (4 layers)	146100	29.22 ± 0.06	39.1 ± 0.1
1 track (3 layers) + extra cluster(s)	2241	0.448 ± 0.009	0.60 ± 0.01
1 track (4 layers) + extra cluster(s)	8467	1.69 ± 0.02	2.27 ± 0.02
2 tracks	3647	0.73 ± 0.01	0.98 ± 0.02
≥ 3 tracks	366	0.073 ± 0.004	0.098 ± 0.005
Sub-Total for events with track(s)	**239807**	**47.97**	**64.2**
Total	**500000**	**100**	**133.9**

extra clusters, which implies that the efficiency of our sTGC prototype is situated around 60%. Once again, we believe this efficiency was affected by the edge effects and the bad channels in the prototype. Fully sized sTGC modules should have a better efficiency.

About 2.1% of all events were reconstructed as a single track while also containing at least one layer with 2 or more clusters. In addition to the 0.7% of events that contain two tracks and 0.1% of events that contain 3 tracks or more, this adds up to 2.9% of all events that could potentially be the result of δ-rays. This value is in relative agreement with the expected δ-ray production of 2.3% by muons traversing a 1m thick concrete slab (see appendix A).

In order to study the effect of the value of the trigger timeout window (defined in section 3.3.3) on the distribution of events, subsequent runs were taken with different windows. The rate of double independent muon coincidence in the sTGC quadruplet should scale with the trigger timeout window. Indeed, cosmic muons follow a Poisson distribution, and extending the time over which an

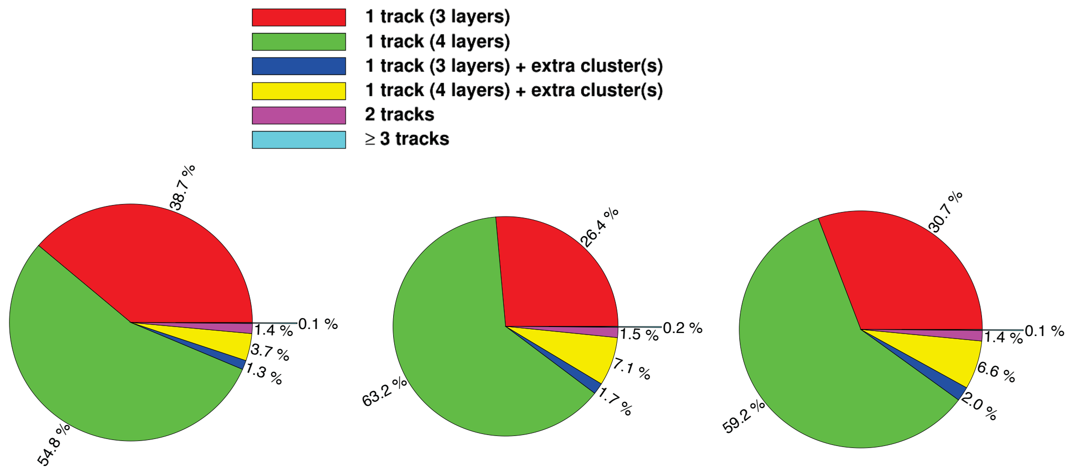

(a) Run with nominal timeout window of 3μs. **(b)** Run with timeout window of 6μs. **(c)** Run with timeout window of 12μs.

Figure 5.4: Effect of trigger timeout value on the distribution of categories of cosmic ray events. Detailed results of the analysis for each run are shown in table 5.2. The cluster position distribution plots for each of these runs is shown in appendix B.

event is recording would increase the expected number of muons within this time. However, it was also known that the probability of having two cosmic muons coincide in the sTGC within 3μs was very low (see section 4.4.1), so doubling this value should not have a visible impact. As for δ-rays, since they are timed with the initial cosmic muon that produced them, extending the trigger timeout window should not increase their rate significantly. Indeed, the only way their rate would increase is if two independent muons produce a δ-ray in the sTGC at the same time, which is highly improbable. Hence, globally, the distribution should stay roughly the same.

The first run (MG0156) kept the standard window value of 3μs, two runs, MG0157 and MG0158, respectively used values of 6μs and 12μs. Since no run lasted exactly the same time (and the value of the trigger timeout window impacts the recording rate), not all data runs contained the same number of events.

Table 5.2: Distribution of events for runs with different trigger timeout windows (excluding trackless events).

MG0156 (timeout 3μs)	**Events / 769424**	**%**	**Rate (Hz)**
1 track (3 layers)	133415	38.41 ± 0.08	23.48 ± 0.06
1 track (4 layers)	191298	55.08 ± 0.08	33.66 ± 0.07
1 track (3 layers) + extra cluster(s)	4359	1.26 ± 0.02	0.78 ± 0.01
1 track (4 layers) + extra cluster(s)	12993	3.74 ± 0.03	2.29 ± 0.02
2 tracks	4755	1.37 ± 0.02	0.84 ± 0.01
≥ 3 tracks	486	0.14 ± 0.01	0.086 ± 0.004
Sub-Total for events with track(s)	**347306**	**100**	**61.2**
MG0157 (timeout 6μs)	**Events / 478480**	**%**	**Rate (Hz)**
1 track (3 layers)	62107	26.40 ± 0.09	19.6 ± 0.1
1 track (4 layers)	148601	63.2 ± 0.1	37.7 ± 0.1
1 track (3 layers) + extra cluster(s)	3906	1.66 ± 0.03	1.24 ± 0.02
1 track (4 layers) + extra cluster(s)	16788	7.14 ± 0.05	4.22 ± 0.04
2 tracks	3500	1.49 ± 0.02	0.90 ± 0.02
≥ 3 tracks	368	0.16 ± 0.01	0.092 ± 0.007
Sub-Total for events with track(s)	**235270**	**100**	**67.6**
MG0158 (timeout 12μs)	**Events / 290696**	**%**	**Rate (Hz)**
1 track (3 layers)	41904	30.7 ± 0.1	11.38 ± 0.06
1 track (4 layers)	80766	59.2 ± 0.1	21.94 ± 0.08
1 track (3 layers) + extra cluster(s)	2665	1.95 ± 0.04	0.72 ± 0.01
1 track (4 layers) + extra cluster(s)	9038	6.62 ± 0.07	2.45 ± 0.03
2 tracks	1937	1.42 ± 0.03	0.53 ± 0.01
≥ 3 tracks	198	0.15 ± 0.01	0.054 ± 0.004
Sub-Total for events with track(s)	**136508**	**100**	**63.8**

Respectively 769424, 497480 and 290696 events have been analyzed for MG0156, MG0157 and MG0158. The resulting event distribution for each run can be seen in table 5.2 and figure 5.4. We can see that as the trigger window is doubled, the number of events with 1 track made of 3 clusters reduces by 12.3%, in favor mostly of events with 1 track and 4 clusters ($+8.4\%$) and events with one track and extra clusters ($+3.8\%$). This suggests that a timeout window of 6μs is better at forming 4 layer tracks than the nominal timeout window of 3μs. However, interestingly, the number of events containing 2 tracks remained almost constant. The 3.6% increase of extra cluster events seems to contradict the initial hypothesis we formed above and instead suggests that some fraction of the extra clusters originate from "noise" of some sort rather than δ-rays.

Increasing the trigger timeout window from 3μs to 12μs does not seem to affect the proportion of events containing 2 tracks. This confirms that this category is associated with δ-rays (or something similar), since we didn't expect such events to scale with the value of the timeout window. One of the categories that scales well with the trigger timeout window is the single-track multi-cluster category (blue). This shows that one source of clusters scales with the trigger timeout window. Since we know the probability of having two independent muons within one event is very small (see section 4.4.1), this source is probably "noise" of some sort.

As for the rate of recording events containing one track or more, no obvious trend is observed. With a rate of 64.2Hz for MG0148 (window of 3μs), 61.2Hz for MG0156 (3μs), 67.6Hz for MG0157 (6μs) and 63.8Hz for MG0158 (12μs), it seems the value of the trigger timeout window does not directly affect the rate. This suggests the 40×60cm^2 sTGC prototype is probably fully efficient for muons and is not greatly affected by fake hits, noise, or double muon coincidence within a same event, as expected. If it was affected by such things, the rate would have increased along with the trigger timeout window. Thus, this reinforces that the multi-track events observed in the detector are δ-rays, since their rate is not expected to change with the trigger timeout window.

It should be mentioned that the recording rates of the runs discussed above vary by more than their quoted statistical uncertainty. This shows there are some systematics we do not yet fully understand, most likely inside the electronics system. For example, it is possible that the readout electronics have time-dependent sensitivities that could explain these variations, along with the peaks in cluster position distributions seen in figures B.2 and B.3.

6

Conclusion and Outlook

Cosmic ray events have been recorded from a $40 \times 60 \text{cm}^2$ sTGC detector in the McGill sTGC testbench, and those reconstructed with two tracks or more have been specifically studied. This population of multi-cluster events is many orders more than the expected rate from random muon coincidence, but is consistent with expectations from delta ray production in a concrete ceiling. Different categories of multi-cluster events have been defined. It was observed that the population of these categories shifts with the value of the trigger timeout window, but this measurement is limited by systematics related to the detector electronics. A trigger timeout window of 6μs might provide better measurements than the nominal window of 3μs, since the former produces more tracks containing data on all layers of the detector, however this will need to be studied using the final electronics. Also, by doubling the value of the trigger timeout window, the number of multi cluster events is doubled. However, this effect seems to be non-linear, since quadrupling the standard trigger timeout window does not quadruple the number of double cluster events. Future work could include comparison with a Monte Carlo simulation of cosmic rays entering an sTGC quadruplet. While such a simulation exists in a preliminary stage, the detector electronics is not part of it. Adding the electronics to the simulation would be useful in understanding exactly what multi-cluster events could be made of, and determine which process ends up forming which kind of multi-track event in a physical detector. The study could also be repeated using a full-size sTGC module and upgraded electronics when they become available, but using the same multi-cluster track reconstruction algorithm.

This study provided indirect cross-checks of certain aspects of the main single-cluster analysis, such as the different data cleaning cuts used and track reconstruction. It also gave a better insight into ways that some multi-cluster events might be used to enhance primary characterization techniques employed by the McGill testing facility.

A

Simulation of δ-ray production for the McGill sTGC Testbench

As discussed in section 4.4.1, the rate of multi-cluster events measured by the $40 \times 60\text{cm}^2$ sTGC detector in the McGill sTGC Testbench was 5.56×10^6 times higher than what could be predicted using basic calculations. One of the hypotheses that was formulated to explain this discrepancy was that the prototype sTGC quadruplet in the testbench recorded many events containing δ-rays, as opposed to two independent muons. These δ-rays are energetic enough ($\gtrsim$ 1MeV) to be detected by an sTGC. However, no simple calculation could be done to estimate the rate of δ-rays that should be expected in the testing facility. Since the sTGC testbench is located on the second floor of the Rutherford Building (4 floors total), it was thought that most of the δ-rays would be a result of the passage of muons through concrete.

Using software known as GEANT4 [43] [44], one can simulate the passage of particles through matter. In this case, we use the software to simulate the passage of muons through concrete in order to determine the probability of forming a δ-ray that could be detected with an sTGC detector [46]. The concrete was simulated to be 1m thick and very wide in order to negate edge effects. The incident muons were given a kinetic energy of 1GeV with a downward orientation and placed at

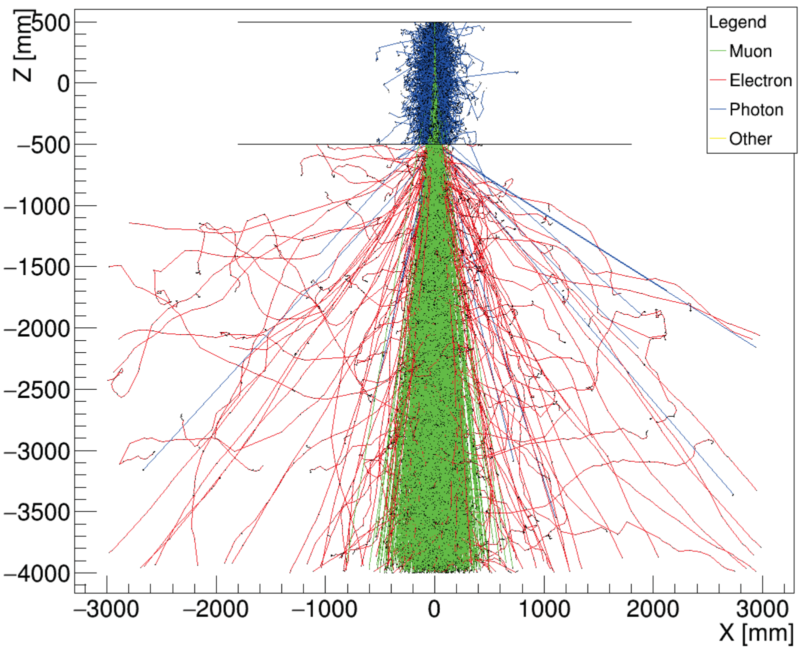

Figure A.1: Event display of 1000 simulated muons traversing 1m thick concrete slab. The electrons and positrons that make it outside the concrete are δ-ray candidates (before cuts).

the surface of the concrete slab. Figure A.1 displays the resulting particles after the passage of 1000 muons through the concrete slab. The energy distribution of 1×10^5 muons that traverse the concrete slab is plotted in figure A.2, with a mean energy of 584.5MeV.

In this simulation, a selection is made over the electrons and positrons ($e^{\pm}$) to determine which ones are sTGC detectable δ-ray candidates. The first cut requires the $e^{\pm}$ produced within the concrete slab to fully traverse it. This is straightforward: if an $e^{\pm}$ loses all its energy before exiting the concrete slab, there is no way it can make it to an sTGC detector below the slab. The second cut requires $T_{e^{\pm}} > 1$MeV. This is to ensure the selected δ-ray candidates have a sufficient kinetic energy to be detected by an sTGC detector. The third and final cut requires the $e^{\pm}$ to have a track straightness of $s > 0.98$. The straightness s is defined as

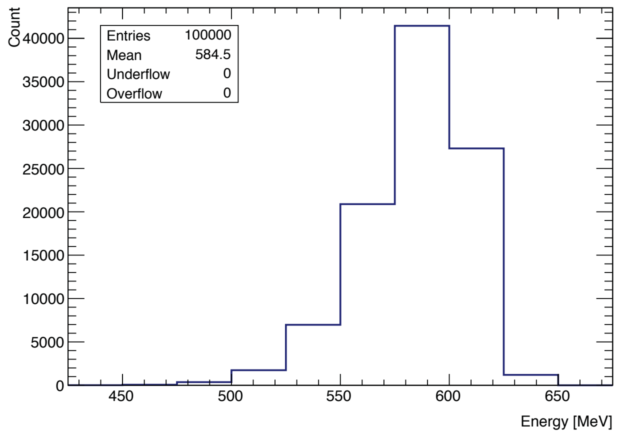

Figure A.2: Energy distribution for muons traversing 1m thick concrete slab

$$s = \frac{trackdistance}{tracklength} \tag{A.1}$$

where the track length is defined as the sum of the distances between all points in a track. This final cut ensures that the $e^{\pm}$ travels in a fairly straight line, as opposed to a spiral. The reason we apply this cut is because the multi-cluster algorithm described in section 4.4.2 reconstructs events with linear fits since it expects the particles going through the sTGC detector to travel in a straight line. The energy spectrum of the δ-ray candidates is plotted in figure A.3 for each of these cuts.

Finally, figure A.4 shows the number of δ-ray candidates (after all the cuts) produced by 1×10^5 independent muons. In total, 2333 δ-ray candidates have been produced, which equates to a probability of 2.33% of forming a δ-ray for each muon.

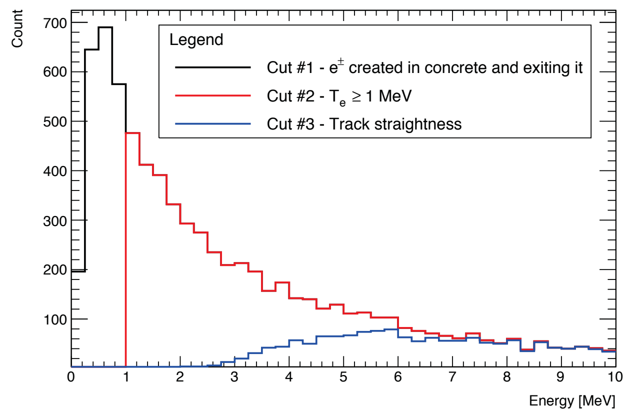

Figure A.3: Cuts for identifying δ-rays in GEANT simulation

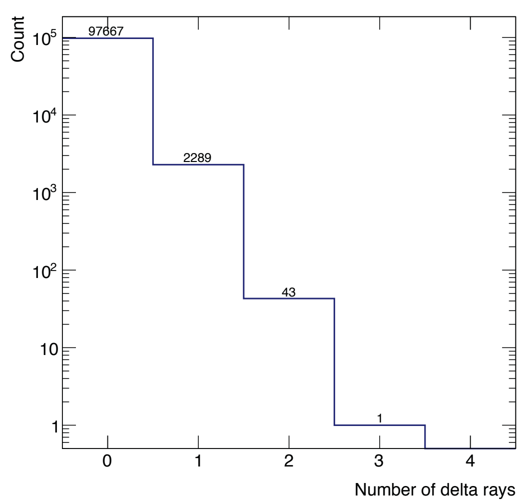

Figure A.4: Number of δ-rays per muon in simulation, for 10^5 muons.

B

Cluster Position Distributions for Runs with Modified Trigger Timeout Windows

This section shows the cluster position distribution for runs with a modified trigger timeout window (MG0156, M0157 and MG0158). The distributions for windows of 3μs, 6μs and 12μs are respectively plotted in figure B.1, B.2 and B.3. Since the electronic setup is exactly the same for each run, the bad channels are also the same for each run (34 and 55 for layer 1, 2 and 11 for layer 2, 8, 25 and 49 for layer 3 and 48 for layer 4). The raw hits distribution (red) and the cluster positions prior to cluster cuts (green) seem to be fairly similar from run to run, but the final cluster position for events that contained reconstructed tracks (cyan) do not stay constant. The distribution of cluster position for clusters part of reconstructed tracks (yellow) features no change from the final cluster positions (cyan). The runs with an extended trigger timeout window seem to feature peaks on noise on most layers on specific channel ranges.

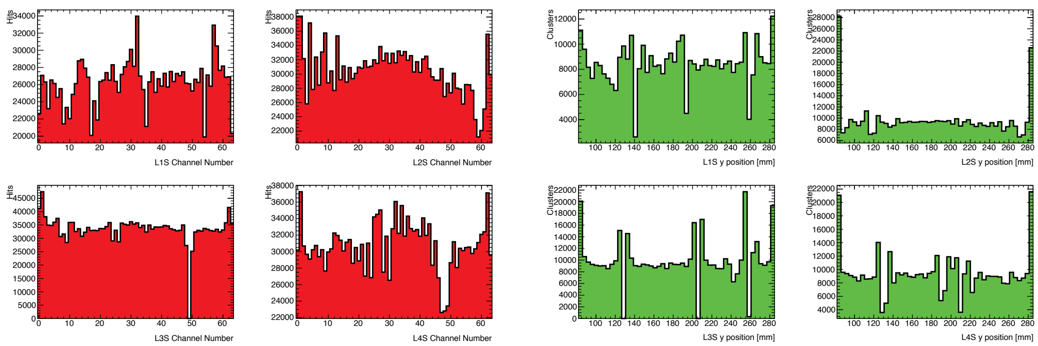

(a) Distribution of the location of recorded hits before pre-selection cuts.

(b) Distribution of cluster positions prior to cluster cuts.

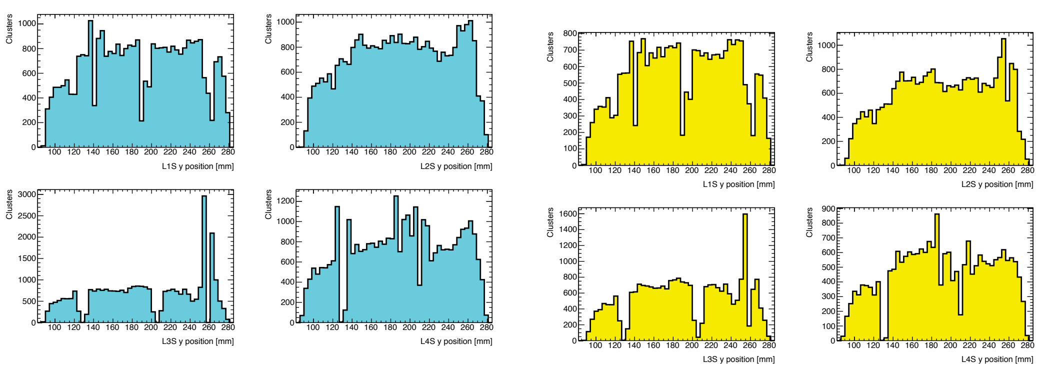

(c) Distribution of the position of clusters part of an event with at least one fitted track.

(d) Distribution of the position of clusters on a fitted track.

Figure B.1: Position distribution of hits and clusters with a nominal trigger timeout of 3μs (MG0156). The bad channels are 34 and 55 for layer 1, 2 and 11 for layer 2, 8, 25 and 49 for layer 3 and 48 for layer 4.

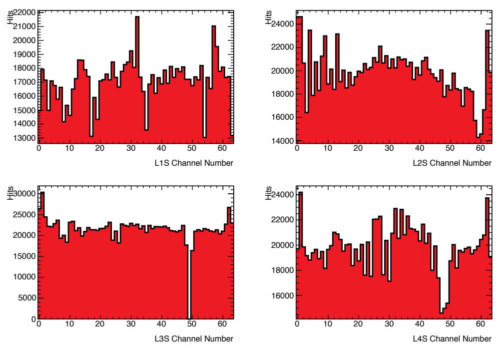

(a) Distribution of the location of recorded hits before pre-selection cuts.

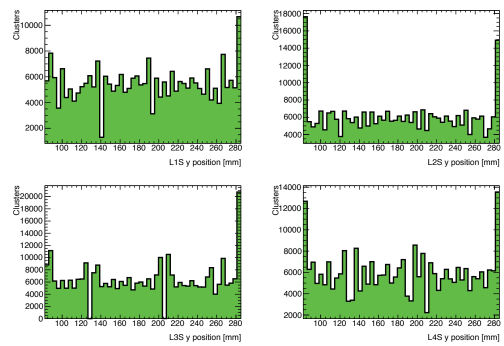

(b) Distribution of cluster positions prior to cluster cuts.

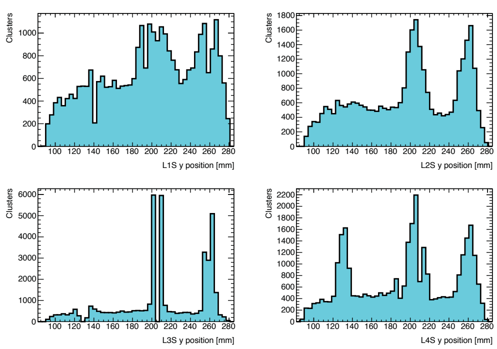

(c) Distribution of the position of clusters part of an event with at least one fitted track.

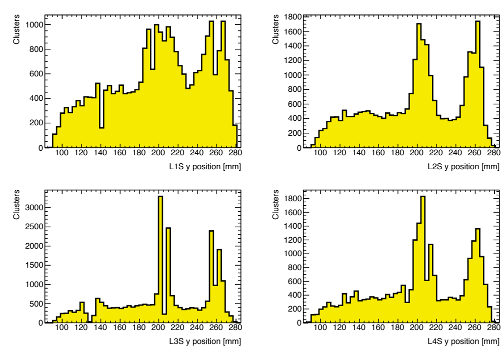

(d) Distribution of the position of clusters on a fitted track.

Figure B.2: Position distribution of hits and clusters with a trigger timeout window of 6μs (MG0157). The bad channels are the same as those in figure B.1

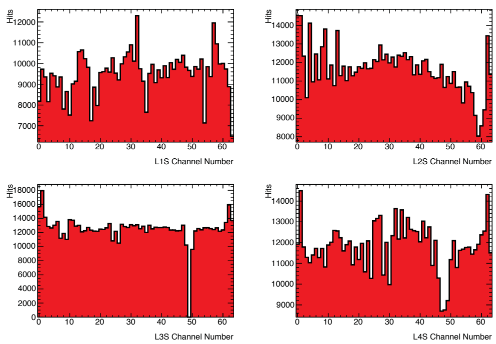

(a) Distribution of the location of recorded hits before pre-selection cuts.

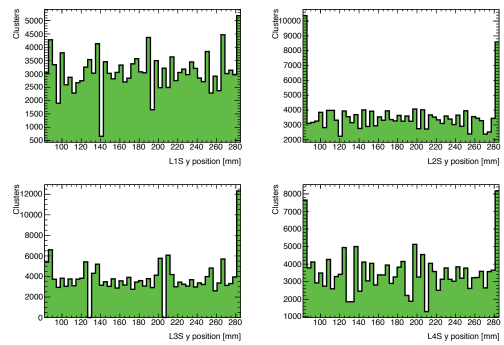

(b) Distribution of cluster positions prior to cluster cuts.

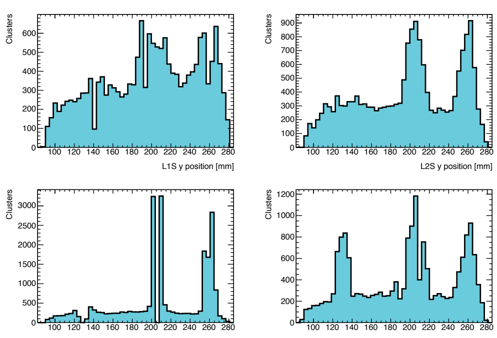

(c) Distribution of the position of clusters part of an event with at least one fitted track.

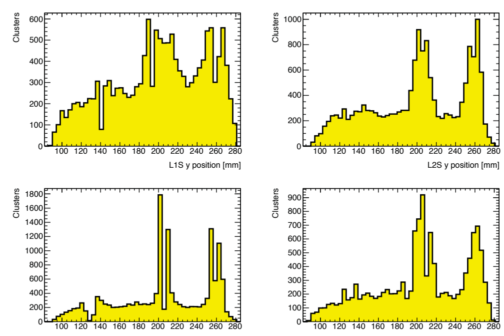

(d) Distribution of the position of clusters on a fitted track.

Figure B.3: Position distribution of hits and clusters with a trigger timeout window of 12μs (MG0158). The bad channels are the same as those in figure B.1

Bibliography

[1] S. F. Novaes. Standard model: An Introduction. In *Particles and fields. Proceedings, 10th Jorge Andre Swieca Summer School, Sao Paulo, Brazil, February 6-12, 1999*, pages 5–102, 1999.

[2] The ATLAS Collaboration. The ATLAS Experiment at the CERN Large Hadron Collider. *Journal of Instrumentation*, 3:S08003, 2008.

[3] Lyndon Evans and Philip Bryant. LHC Machine. *Journal of Instrumentation*, 3:S08001, 2008.

[4] B. Stelzer and the ATLAS Muon Collaboration. The New Small Wheel Upgrade Project of the ATLAS Experiment. *Nucl. Part. Phys. Proc.*, 273-275:1160–1165, 2016.

[5] R. Keyes, K.A. Johnson, L. Pepin, F. Léger, C. Qin, S. Webster, A. Robichaud-Véronneau, C. Bélanger-Champagne, B. Lefebvre, S.H. Robertson, A. Warburton, B. Vachon and F. Corriveau. Development and characterisation of a gas system and its associated slow-control system for an ATLAS small-strip thin gap chamber testing facility. *Journal of Instrumentation*, 12(04):P04027, 2017.

[6] Sheldon L. Glashow. Partial-symmetries of weak interactions. *Nuclear Physics*, 22(4):579 – 588, 1961.

[7] Steven Weinberg. A Model of Leptons. *Phys. Rev. Lett.*, 19:1264–1266, Nov 1967.

[8] Abdus Salam. Elementary Particle Physics: Relativistic Groups and Analyticity. page 367. Stockholm: Almqvist & Wiksell, 1968. Proceedings of the eigth Nobel symposium.

[9] Peter W. Higgs. Broken Symmetries and the Masses of Gauge Bosons. *Phys. Rev. Lett.*, 13:508–509, Oct 1964.

[10] David J. Gross and Frank Wilczek. Ultraviolet Behavior of Non-Abelian Gauge Theories. *Phys. Rev. Lett.*, 30:1343–1346, Jun 1973.

[11] J.J. Aubert et al. Experimental Observation of a Heavy Particle J. *Phys. Rev. Lett.*, 33:1404–1406, Dec 1974.

[12] Dmitry Kazakov. The Higgs Boson is found: what is next? *Phys. Usp.*, 57(9):930–942, 2014. [Usp. Fiz. Nauk184,no.9,1004(2014)].

[13] V.K. Shen, D.W. Siderius, W.P. Krekelberg and H.W. Hatch. NIST Standard Reference Simulation Website. *NIST Standard Reference Database*, 173. `http://doi.org/10.18434/T4M88Q` (accessed February 28, 2017).

[14] C. Patrignani et al. Review of Particle Physics. *Chin. Phys.*, C40(10):100001, 2016.

[15] G. Arnison et al. Experimental Observation of Isolated Large Transverse Energy Electrons with Associated Missing Energy at $\sqrt{s}$ = 540-GeV. *Phys. Lett.*, 122B:103–116, 1983. [,611(1983)].

[16] P. Bagnaia et al. Evidence for $Z^0 \to e^+e^-$ at the CERN anti-p p Collider. *Phys. Lett.*, 129B:130–140, 1983.

[17] David J Griffiths. *Introduction to elementary particles; 2nd rev. version*. Physics textbook. Wiley, New York, NY, 2008.

[18] The ATLAS Collaboration. Observation of a new particle in the search for the Standard Model Higgs boson with the ATLAS detector at the LHC. *Phys. Lett.*, B716:1–29, 2012.

[19] John Baez. *How Many Fundamental Constants Are There?*, 2011. `http://math.ucr.edu/home/baez/constants.html` (accessed January 5, 2017).

[20] Gianfranco Bertone, Dan Hooper, and Joseph Silk. Particle dark matter: Evidence, candidates and constraints. *Phys. Rept.*, 405:279–390, 2005.

[21] Hans Peter Nilles. Supersymmetry, Supergravity and Particle Physics. *Phys. Rept.*, 110:1–162, 1984.

[22] Hörandel, Jörg R. Early Cosmic-Ray Work Published in German. 2012. [AIP Conf. Proc.1516,52(2012)].

[23] Rod Nave. *HyperPhysics*, 1999. `http://hyperphysics.phy-astr.gsu.edu/hbase/Astro/cosmic.html` (accessed December 16, 2016).

[24] NASA. *Cosmic Rays*, 2011. http://imagine.gsfc.nasa.gov/science/objects/cosmic_rays2.html (accessed December 16, 2016).

[25] M. Ackermann et al. Detection of the Characteristic Pion-Decay Signature in Supernova Remnants. *Science*, 339:807, 2013.

[26] E.B. Podgoršak and International Atomic Energy Agency. *Radiation Oncology Physics: A Handbook for Teachers and Students*. STI/PUB. International Atomic Energy Agency, 2005.

[27] The LHC accelerator complex. https://home.cern/about/accelerators (accessed July 18 2017).

[28] O. Brüning et al. *LHC Design Report*. CERN Yellow Reports: Monographs. CERN, Geneva, 2004.

[29] The LHC is back, Nov 2009. http://press.cern/press-releases/2009/11/lhc-back (accessed July 18 2017).

[30] Joao Pequenao. Computer generated image of the whole ATLAS detector, Mar 2008. http://cds.cern.ch/record/1095924 (accessed February 22, 2017).

[31] The ATLAS Collaboration. ATLAS pixel detector electronics and sensors. *Journal of Instrumentation*, 3(07):P07007, 2008.

[32] I. Gorelov et al. A measurement of Lorentz angle and spatial resolution of radiation hard silicon pixel sensors. *Nuclear Instruments and Methods in Physics Research Section A: Accelerators, Spectrometers, Detectors and Associated Equipment*, 481(13):204 – 221, 2002.

[33] F. Campabadal et al. Beam tests of ATLAS SCT silicon strip detector modules. *Nuclear Instruments and Methods in Physics Research Section A: Accelerators, Spectrometers, Detectors and Associated Equipment*, 538(1):384 – 407, 2005. `http://www.sciencedirect.com/science/article/pii/S0168900204021059`.

[34] Bartosz Mindur. ATLAS Transition Radiation Tracker (TRT): Straw Tubes for Tracking and Particle Identification at the Large Hadron Collider. Technical Report ATL-INDET-PROC-2016-001, CERN, Geneva, Mar 2016. `https://cds.cern.ch/record/2139567`.

[35] Ana Maria Henriques Correia. The ATLAS Tile Calorimeter. Technical Report ATL-TILECAL-PROC-2015-002, CERN, Geneva, Mar 2015. `https://cds.cern.ch/record/2004868`.

[36] A. Ruiz-Martinez and ATLAS Collaboration. The Run-2 ATLAS Trigger System. Technical Report ATL-DAQ-PROC-2016-003, CERN, Geneva, Feb 2016.

[37] A. Abusleme et al. Performance of a full-size small-strip thin gap chamber prototype for the ATLAS new small wheel muon upgrade. *Nucl. Instrum. Meth. Research Section A: Accelerators, Spectrometers, Detectors and Associated Equipment*, 817:85 – 92, 2016. `http://www.sciencedirect.com/science/article/pii/S0168900216001285`.

[38] S. Majewski, Georges Charpak, A. Breskin, and G. Mikenberg. A Thin Multiwire Chamber Operating In The High Multiplication Mode. *Nucl. Instrum. Meth.*, 217:265–271, 1983.

[39] Walter Blum, Luigi Rolandi, and Werner Riegler. *Particle detection with drift chambers*. Particle Acceleration and Detection. 2008.

[40] Estel Perez Codina. Small-Strip Thin Gap Chambers for the Muon Spectrometer Upgrade of the ATLAS Experiment. Technical Report ATL-MUON-PROC-2015-004, CERN, Geneva, Jun 2015.

[41] Gianluigi De Geronimo, Jack Fried, Shaorui Li, Jessica Metcalfe, Neena Nambiar, Emerson Vernon, and Venetios Polychronakos. VMM1 - An ASIC for Micropattern Detectors. *IEEE Trans. Nucl. Sci.*, 60:2314–2321, 2013.

[42] Benoit Lefebvre, Camille Belanger-Champagne, Andrée Robichaud-Véronneau, and Brigitte Vachon. Study of pedestal measurement methods for VMM1 ASICs. Technical Report ATL-COM-UPGRADE-2016-003, CERN, Geneva, Feb 2016.

[43] S. Agostinelli et al. GEANT4, a simulation toolkit. *Nuclear Instruments and Methods in Physics Research Section A: Accelerators, Spectrometers, Detectors and Associated Equipment*, 506(3):250 – 303, 2003.

[44] J. Allison et al. GEANT4 developments and applications. *IEEE Transactions on Nuclear Science*, 53(1):270–278, Feb 2006.

[45] Sean Wallis. Binomial Confidence Intervals and Contingency Tests: Mathematical Fundamentals and the Evaluation of Alternative Methods. *Journal of Quantitative Linguistics*, 20(3):178–208, 2013.

[46] Private communication with Jonathan Larochelle, McGill University, July 2017.